BAMS Article

Desert–Oasis Convergence Line and Deep Convection Experiment (DECODE)

Zhiyong Meng,[a] Xuefeng Meng,[b] Chenggang Wang,[c] Yipeng Huang,[d] Shuhao Zhang,[e] Hongjun Liu,[f,a] Murong Zhang,[g] Yijing Liu,[h] Hao Huang,[i] Lijuan Su,[j] Quxin Cui,[a] Feng Lu,[k] Kun Zhao,[i] Lei Zhu,[l] Li Wang,[e] Zhihua Zhou,[b] Linchun Liu,[b] Xuefeng Ma,[b] Jiutao Shan,[m] Yao Xiao,[j] Daoru Zhu,[b] Zhengwei Yang,[i] Xucheng Zheng,[j] Fan Bo,[i] Lanqiang Bai,[n] Xiaojuan Yao,[b] Yonggang Sun,[b] Manyun Lin,[k] Zimeng Zheng,[a] Liao Zhou,[c] Xuelei Wang,[a] Ke Liu,[b] Luyi Chen,[a] Lebao Yao,[o,b] Ming Guan,[c] Weikang Kong,[c] Shaoyang Sun,[c] Jiaxin Wang,[c] Yikai Wu,[c] Yaqi Qin,[c] Xiaoying Jiang,[c] Xiang Pan,[i] Mufei Wang,[i] Changan Zhang,[i] Yanjun Tuo,[p] Hanchao Li,[j] Hui Li,[j] Lixia Shi,[e] Xiaohong Fang,[e] Feng Zhu,[b] Xin Sun,[b] Jingbo Yun,[b] Shiyun Liu,[q] Huiqing Wang,[b] Yawen Yang,[r,a] Jingyi Wen,[a] Peiyu Wang,[a] Lanbo Liu,[s] Nan Ren,[e] Xiufeng Wu,[t] Zhengyue Zhang,[u] Jianyu Pei,[v] Zhi Yang,[u] and Cheng Xia[w,u]

KEYWORDS:
Complex terrain;
Convection lines;
Convective-scale processes;
Boundary layer;
Vegetation;
Orographic effects

ABSTRACT: The heterogeneous land surface spanning the Yellow River irrigated oasis and the adjacent Kubuqi and Ulan Buh Desert (Hetao area) in Inner Mongolia, China, has been noted to frequently generate planetary boundary layer convergence line (BLCL), providing an important source of low-level lifting for convection initiation (CI). As the first field experiment to collect comprehensive observations of vegetation-contrast-resulting thermal circulations that consistently generate BLCLs and lead to CI, the Desert–Oasis Convergence Line and Deep Convection Experiment (DECODE) was conducted from 5 July to 9 August 2022 in the Hetao area. Two oasis and four desert observation sites were set up in the region that exhibits the highest frequency of BLCL and CI occurrences, equipped with a suite of advanced instruments probing land–atmosphere interactions, planetary boundary layer processes, and evolution of BLCLs and their associated CI, including Doppler lidars, microwave radiometers, soil temperature and moisture sensors, eddy covariance systems, portable radiosondes, C-band polarimetric Doppler radar, aircraft, and Geostationary High-speed Imager onboard *FY-4B* satellite. DECODE captured 29 BLCLs (16 with CI), 66 gust fronts, 12 horizontal convective rolls, and one tornado. The observations unveiled full thermal circulations spanning the desert–oasis boundary characterized by a horizontal width of ~25 km, a convergence height of ~1 km above ground level (AGL), and divergence from 2 to ~3.5 km AGL, with vertical wind speeds of up to 2 m s^{-1}. Future publications stemming from DECODE will delve into a spectrum of scientific inquiries, including but not limited to land surface and boundary layer processes, BLCL dynamics, CI mechanisms, convective organization, predictability, and model evaluation.

DOI: 10.1175/BAMS-D-23-0222.1

Corresponding authors: Zhiyong Meng, zymeng@pku.edu.cn; Chenggang Wang, wcg@nuist.edu.cn

Manuscript received 23 August 2023, in final form 7 August 2024, accepted 30 August 2024

SIGNIFICANCE STATEMENT: The purpose of Desert–Oasis Convergence Line and Deep Convection Experiment (DECODE) is to collect intensive observations around desert–oasis divide to better understand the physical processes of boundary layer convergence lines (BLCLs), their associated thermal circulations, convection initiation (CI), and organization over heterogeneous land surfaces. This is important because deep convection initiation poses a major challenge for weather forecasting over heterogeneous land surfaces due to limited understanding of land–atmosphere interactions. In addition, the targeting divide between a desert and an irrigated oasis facilitates a unique situation where human activities can change the weather. This campaign captured 29 BLCLs (16 with CI), which provided a rich dataset for studies not only on convection dynamics and microphysics but also on land–atmosphere interactions, boundary layer processes, and even interdisciplinary studies such as wind farm impact and convective dust storms.

AFFILIATIONS: [a] Department of Atmospheric and Oceanic Sciences, School of Physics, and China Meteorological Administration Tornado Key Laboratory, Peking University, Beijing, China; [b] Inner Mongolia Meteorological Observatory, Hohhot, China; [c] Key Laboratory for Aerosol-Cloud-Precipitation of China Meteorological Administration, Nanjing University of Information Science and Technology, Nanjing, China; [d] Xiamen Key Laboratory of Straits Meteorology, Xiamen Meteorological Bureau, Xiamen, China; [e] Bayannur Meteorological Bureau of Inner Mongolia, Linhe, China; [f] Institute of Urban Meteorology, Beijing, China; [g] State Key Laboratory of Marine Environmental Science, Center for Marine Meteorology and Climate Change, College of Ocean and Earth Sciences, Xiamen University, Xiamen, China; [h] Jiangxi Storm Chasing Videos Culture Co. Ltd., Nanchang, China; [i] Key Laboratory for Mesoscale Severe Weather, Ministry of Education and School of Atmospheric Sciences, Nanjing University, Nanjing, China; [j] Inner Mongolia Weather Modification Center, Hohhot, China; [k] National Satellite Meteorological Center, Beijing, China; [l] Key Laboratory of Meteorological Disaster, Nanjing University of Information Science and Technology, Nanjing, China; [m] Key Laboratory for Weather Modification of Inner Mongolia, Meteorological Science Institute of Inner Mongolia, Hohhot, China; [n] Foshan Tornado Research Center, and China Meteorological Administration Tornado Key Laboratory, Guangdong Meteorological Service, Guangdong, China; [o] School of Atmospheric Sciences, Guangdong Province Key Laboratory for Climate Change and Natural Disaster Studies, Sun Yat-sen University, Zhuhai, China; [p] Linhe District Meteorological Bureau of Bayannur, Linhe, China; [q] Ulanqab Meteorological Bureau of Inner Mongolia, Ulanqab, China; [r] Institute of Atmospheric Physics, Chinese Academy of Sciences, Beijing, China; [s] Baotou Meteorological Bureau of Inner Mongolia, Baotou, China; [t] Ordos Meteorological Bureau of Inner Mongolia, Ordos, China; [u] Dengkou County Meteorological Bureau of Bayannur, Dengkou, China; [v] Hangjin Banner Meteorological Bureau of Ordos, Hangjin, Banner China; [w] Alxa League Meteorological Bureau of Inner Mongolia, Alxa Left Banner, China

1. Background

In early October 2016, by fortuitously clicking on a radar image folder labeled “Linhe” on a computer at the Training Center of the China Meteorological Administration, the first author stumbled upon a captivating series of convection initiation (CI) processes that occurred over three consecutive days in early June 2013 (e.g., Figs. 1a–d for 4 June 2013) at similar local times and locations. Specifically, around 0800 local standard time (LST = UTC + 8 h), a distinct radar fine line of reflectivity at 0.5° or 1.5° elevation emerged approximately 50 km south of the Linhe Radar (LHRD), gradually extending northeastward while drifting slightly eastward. By approximately 1400 LST, convective cells began to develop along the fine line, progressively

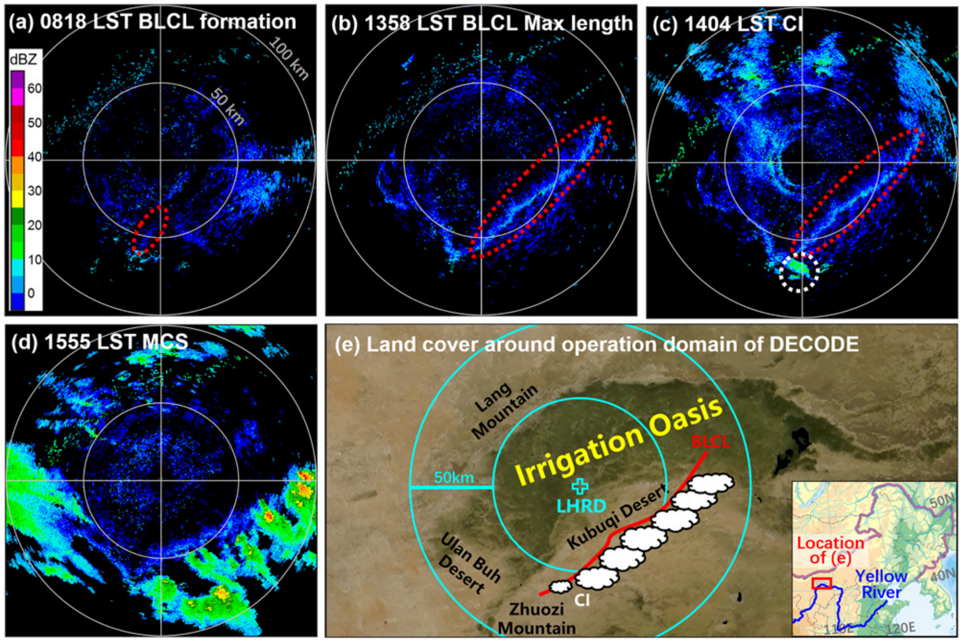

Fig. 1. **Composite reflectivity obtained from the lowest two elevations (0.5° and 1.5°) of the LHRD at (a) 0818 LST 4 Jun 2013 for the BLCL formation and (b) 1358 LST 4 Jun 2013 for the BLCL reaching its maximum length. Composite reflectivity from all nine elevations during the CI phase are shown at (c) 1404 and (d) 1555 LST 4 Jun 2013. (e) A clear-air FY-3 image showing the terrain surrounding the LHRD and the general location of BLCL (red line) and CI (white clouds). The location of (e) is denoted by the red box in its inset map located in the lower-right corner. The Yellow River is denoted by the blue contour in the inset map of (e).**

merging to form a mesoscale convective system (MCS). Upon scrutinizing LHRD images spanning the entire summer of 2013, it became apparent that similar CI events occurred with notable frequency. This unveiled a wealth of CI phenomena associated with planetary boundary layer convergence lines (BLCLs) over a unique land-cover mosaic encompassing irrigated oasis, deserts, the Yellow River, and mountain regions (Fig. 1e). Subsequent investigations unfolded naturally. Based on 5 years of LHRD data and ERA5 reanalysis, statistical analyses were conducted on BLCLs and their associated convective precipitations (Huang et al. 2019), as well as their dominant synoptic patterns (Huang et al. 2022). A numerical simulation was performed to elucidate a typical case (Liu et al. 2023). This research endeavor was then underpinned by a key project funded in 2021 by the National Natural Science Foundation of China. One major goal of this key project is to conduct the Desert–Oasis Convergence Line and Deep Convection Experiment (DECODE).

The initiation of deep convection poses a major challenge for weather forecasting, owing to the limited understanding of land–atmosphere interactions. CI results from a complex interplay of moisture, instability, and lifting, thereby being closely related to the vertical exchange of moisture and energy among land, vegetation, and atmosphere. However, conventional observational networks inadequately capture these land surface and boundary layer processes, consequently leading to their inadequate representation in numerical models.

Inhomogeneity in soil moisture and vegetation cover has been demonstrated to have an apparent impact on the location of CI. Based on satellite observations, Taylor et al. (2007) demonstrated the apparent impact of uneven soil moisture distribution, particularly at scales of 10–40 km, on CI in the Saharan region. Their findings revealed that regions with pronounced gradients of soil moisture exhibit a doubled probability of CI compared to areas with uniform soil moisture distribution. Building upon this, Taylor et al. (2012) extended the analysis globally, highlighting a tendency for afternoon rainfall to concentrate over drier soil patches. Similar preferences for convection over drier soil have been observed across various regions worldwide, including the United States (Yuan et al. 2020), South America (Chug et al. 2023), West Africa (Klein and Taylor 2020), and Europe (Taylor 2015). However, despite these insightful satellite-based studies, there remains a notable dearth of near-surface and PBL observational evidence.

Given the limited observations, our understanding on the mechanism underlying the impact of uneven soil moisture on CI is mainly based on idealized numerical simulations. Results showed that this impact primarily revolves around the generation of mesoscale thermal circulation induced by uneven surface fluxes. Specifically, drier regions tend to exhibit higher sensible heat fluxes compared to wetter areas, generating ascending motion in dry, warm areas and descending motion in moist, cool regions. Consequently, moisture is transported near the surface from wet to dry regions, where it converges and ascends, ultimately initiating convection (Kang and Bryan 2011; Kang and Ryu 2016). The formation of such thermal circulations can be affected by the magnitude of environmental winds and the magnitude and spatial extent of soil moisture gradients. Froidevaux et al. (2014) demonstrated that in the absence of environmental winds, convection tends to initiate over dry areas, with resultant precipitation predominantly falling within those regions. Under weak environmental wind conditions, convection tends to propagate downstream relative to the prevailing wind direction, originating from the center of dry regions and often precipitating in adjacent wet areas. Given the typically weak nature of thermal circulations induced by soil moisture contrast, excessive environmental winds could hinder their formation. Results from large-eddy simulation indicate that thermal circulations typically occur when environmental winds are below 2 m s^{-1} (Lee et al. 2019). Despite these insights gleaned from idealized modeling studies, the applicability of such findings to real-world scenarios warrants further investigation.

Several field experiments conducted at the end of the last century investigated the impact of heterogeneous land surfaces on boundary layer dynamics. These include the Boardman Regional Flux Experiment (BARFEX; Doran et al. 1992), First ISLSCP Field Experiment (FIFE; Sellers et al. 1988), Hydrologic Atmospheric Pilot Experiment-Modelisation du Bilan Hydrique (HAPEX-MOBILHY) for the Study of Water Budget and Evaporation Flux at the Climatic Scale (André et al. 1986), and the Heihe River Basin Field Experiment (HEIFE; Wang 1999). Recently, the Great Plains Irrigation Experiment (GRAINEX; Rappin et al. 2021) and the Land Surface Interactions with the Atmosphere over the Iberian Semi-Arid Environment campaign (LIAISE; Boone et al. 2021) were launched mainly focusing on the impact of higher soil moisture on PBL features and convective environment in the irrigated area relative to the nonirrigated area (Rappin et al. 2021; Rappin et al. 2022; Lachenmeier et al. 2024; Whitesel et al. 2024; Udina et al. 2024). Most observational evidence till now revealed partial thermal circulations due to soil moisture heterogeneity, such as the irrigation breeze of 500-m depth at irrigated sites in LIAISE (Lunel et al. 2024), irrigation breeze that weakened terrain-generated slope wind in GRAINEX (Phillips et al. 2022), a 200-m-deep farm breeze from the irrigated region to the steppe in BARFEX (Doran et al. 1992), breeze with a frontal updraft about 200 m wide in California Ozone Deposition Experiment (CODE; Mahrt et al. 1994), horizontal convergence in the dry area and divergence in the wet area resulting from a preceding storm in Sahel from the Special Observing Period of the African Monsoon Multidisciplinary Analyses (AMMA; Redelsperger et al. 2006; Taylor et al. 2007) study, and a case in the Interaction of Convective Organization and Monsoon Precipitation, Atmosphere, Surface and Sea (INCOMPASS; Turner et al. 2020) in India (Barton et al. 2020). However, there has been very rare observational evidence of a complete thermal circulation across vegetation contrast, and none explicitly linked the impact of heterogeneous land surfaces to BLCLs and their associated CI.

Conversely, field campaigns like International H_2O Project (IHOP; Weckwerth et al. 2004) and the Understanding Severe Thunderstorms and Alberta Boundary Layers Experiment (UNSTABLE; Taylor et al. 2011) focused on CI but did not prioritize the impact of heterogeneous land surfaces, where boundary layer features over different vegetation covers were mostly observed incidentally rather than systematically.

DECODE marked the first campaign to deliberately examine the influence of vegetation contrast on BLCLs and their associated CI within a semi-arid climate regime. Situated on the north side of the Yellow River bend in Inner Mongolia, China, is the 2200-yr-old Hetao irrigation district, covering 769 333 ha (Fig. 1e). Designated as a World Heritage Irrigation Structure in 2019, this district is surrounded by the Kubuqi Desert to the south, the Ulan Buh Desert to the southwest, and Lang Mountain to the northwest. Consequently, the Hetao area offers compelling real-world evidence of sharp land-cover and land-use contrasts influencing local and regional weather.

According to satellite data analysis by Sato et al. (2007), cumulus clouds are notably less abundant over the oasis compared to the surrounding deserts in the Hetao area. Kawase et al. (2008) corroborated these findings through convection-resolving numerical simulations, illustrating how thermal circulations lead to increased cumulus cloud formation over the desert. Utilizing LHRD data from June to August during 2012–16, Huang et al. (2019) revealed that ~60 BLCLs per year manifest as fine lines of radar reflectivity, predominantly occurring in arid regions along the boundary between the irrigated oasis and adjacent deserts or mountains (Fig. 2a). Of these BLCLs, 44% initiated convection. Notably, a dominant percentage of BLCLs and their associated CI events are concentrated over the Kubuqi Desert, where the desert–oasis contrast is most pronounced. These convective cells occasionally propagate and

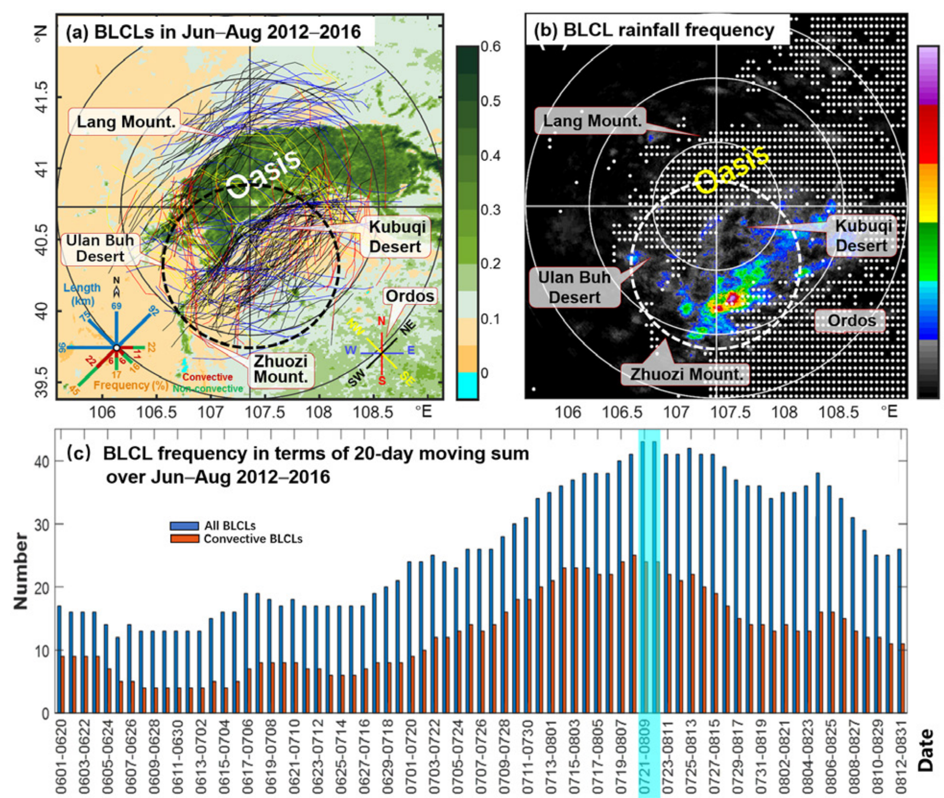

Fig. 2. Distributions of (a) identified BLCLs and (b) associated convective precipitation frequency based on the LHRD observations during 2012–16, adapted from Huang et al. (2019). The dashed circle highlights the focal area of the DECODE project. (c) The 20-day moving sum of all BLCL and convective BLCL frequencies spanning 2012–16, with the two highest peaks in the BLCL occurrence shaded in cyan for emphasis.

intensify downstream (Fig. 2b), leading to severe weather events in northern and eastern China, thereby establishing the Hetao area as a significant “storm generator.”

BLCLs and their associated CI can be greatly influenced by synoptic-scale features, particularly near-surface temperature and ambient flow. Based on ERA5 analyses, Huang et al. (2022) classified the synoptic environments in the Hetao area for June, July, and August from 2012 to 2016 into five patterns, designated as T1–T5 (Fig. 3), with T1 exhibiting the highest frequency. Among these patterns, T1 [in high pressure ridge; Fig. 3a(1)], T4 [in front of a shallow midlevel trough; Fig. 3a(4)], and T5 [in front of a deep midlevel trough; Fig. 3a(5)] are favorable patterns for BLCL formation and CI. These three favorable patterns are characterized by warm near-surface air (Fig. 3b) and southerly winds west to the subtropical high or ahead of the midlevel trough (Fig. 3c), opposing the oasis breeze and creating optimal conditions

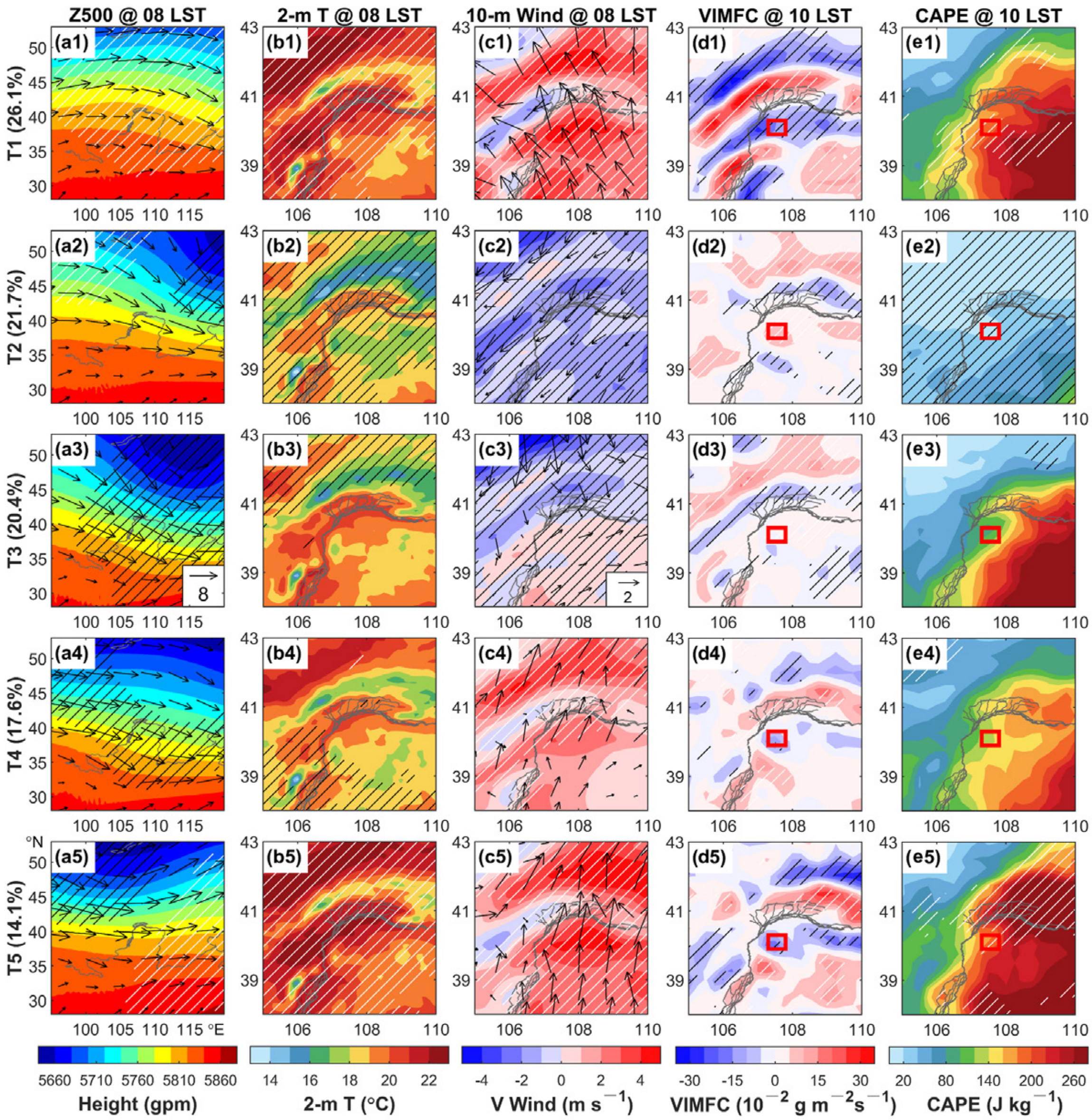

Fig. 3. **ERA5-based composite (a) 500-hPa geopotential height (gpm) and wind (m s^{-1}), (b) 2-m temperature (°C), (c) 10-m wind (m s^{-1}), at 0800 LST, (d) vertically integrated moisture flux convergence (VIMFC; 10^{-2} g m^{-2} s^{-1}), and (e) CAPE (J kg^{-1}) at 1000 LST for the five synoptic patterns during warm seasons from 2012 to 2016. The occurrence frequency of T1–T5 is given on the left-hand side. The Yellow River and irrigation canals are denoted by gray curves. The hatched areas in each panel indicate regions passing the Student’s *t* test at a confidence level of 90%. In (d1–d5) and (e1–e5), the red boxes denote the key areas of convection associated with BLCLs, adapted from Huang et al. (2019). This figure is adapted from Huang et al. (2022).**

of high low-level moisture (Fig. 3d) and instability (Fig. 3e). In contrast, T2 and T3 represent patterns post-midlevel shallow and deep troughs [Figs. 3a(2)–e(2),a(3)–e(3)], respectively, which are considered unfavorable for BLCL formation and CI.

Nevertheless, despite these advancements, the details of BLCL structure and dynamics, and their association with convective processes, alongside the underlying land surface and PBL processes across the desert and oasis interfaces, remain poorly understood due to a dearth of detailed observations. Motivated by this knowledge gap, DECODE was conceived to gather comprehensive observations aimed at unraveling the formation mechanisms of BLCLs and their associated CI processes, leveraging the unparalleled desert–oasis contrast in the Hetao area.

2. Scientific objectives

DECODE had two scientific objectives. The first objective was to understand land–atmosphere interactions, PBL processes, and synoptic environments that lead to BLCL formation, CI, and subsequent convective organization. This goal required observing

1) land surface characteristics and their differences across the desert–oasis boundary such as soil temperature and moisture;
2) diurnal variations in surface heat, momentum, water vapor, and energy fluxes, as well as their differences between desert and oasis regions;
3) vertical structure and diurnal variations of temperature, moisture, and wind within the boundary layer, as well as their differences between desert and oasis regions;
4) dynamic, thermodynamic, and microphysical structures of BLCLs and their associated convection.

The second objective was to evaluate the skill of convection-permitting model in predicting the BLCLs and associated CIs and to improve forecast accuracy for CI and the upscale growth of deep convection by assimilating observations collected through DECODE. To achieve this goal, alongside the operational 3-km regional model utilized by the Inner Mongolia Meteorological Observatory, a real-time 1-km WRF Model was deployed to provide field guidance.

3. Field experiment design and implementation

a. Domain of operation. Statistical analysis of BLCLs (Fig. 2a) and their associated convective precipitation (Fig. 2b) utilizing LHRD data during the summer seasons from 2012 to 2016 reveals that convective precipitation induced by BLCLs predominantly occurs along the boundary between the Kubuqi Desert and the Ordos Grassland. This phenomenon is mainly attributed to convective activity associated with BLCLs at the interface between the oasis and the Kubuqi Desert. Consequently, the delineated dashed elliptical region in Fig. 2a, spanning from 106.75° to 107.75°E and 40° to 40.75°N, was designated as the operational domain for the field campaign.

b. Period of operation. Analysis of the 20-day moving sum of BLCL frequency within the designated domain from 2012 to 2016 (Fig. 2c) indicates that the peak occurrence of BLCLs falls between 9 July and 20 August, with a particularly high frequency observed from 21 July to 9 August. Therefore, the observation period for the DECODE project was selected as 21 July–9 August 2022, with a pilot experiment originally scheduled for 10–20 July 2022. The objective of the pilot experiment was to test and optimize the observation scheme, examining the status of various instruments, especially those at desert sites where power supply facilities could be unstable. Due to preparedness ahead of schedule, the pilot experiment commenced early on 5 July.

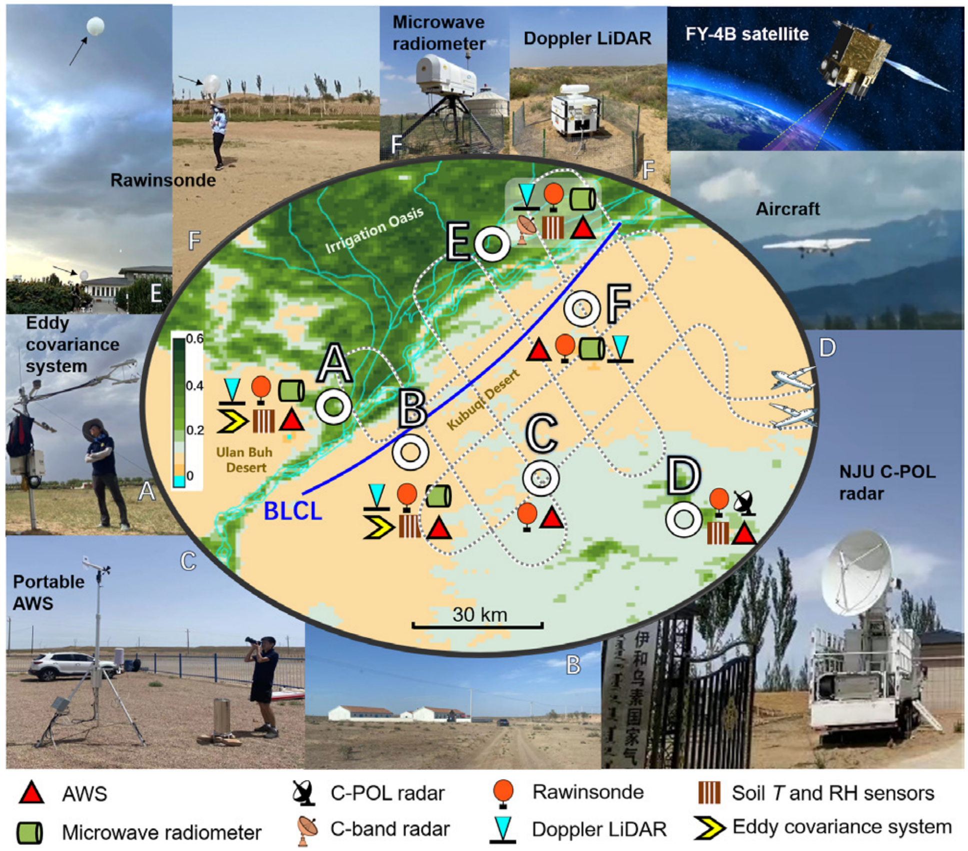

Fig. 4. Distributions of the six observation sites labeled as A, B, C, D, E, and F within the inner ellipse. The blue line represents a schematic depiction of a typical BLCL, while the gray dotted line indicates a typical flight path of the aircraft. The shading denotes the MODIS enhanced vegetation index (EVI; Didan 2015) product MOD13A3. The Yellow River and irrigation canals are denoted by cyan curves. Additionally, the images showcase the deployed instruments and the land cover at each of the six sites.

c. Observation sites. To fulfill our scientific objectives, six observation sites (Fig. 4) were established. Sites A and E were situated over the oasis, characterized by grassland terrain, while sites B and F were positioned over the Kubuqi Desert, featuring desert landscapes. Site C exhibited a transition zone with desertification of grassland, whereas site D was distinguished by desert grassland.

The selection of the six observation sites was guided by several factors, including the frequency and orientation of BLCLs, the geographical delineation between oasis and desert regions, implementation feasibility, and the distribution of current meteorological observing stations. Based on the distribution of BLCL centroids between 21 July and 9 August during 2012–16, two primary centers of high BLCL frequency were identified, represented by brown circles in Fig. 5. Surrounding these centers, observations along the AD and EF axes were strategically positioned to capture cross-sectional views perpendicular to the typical orientation of BLCLs (Fig. 4). Similarly, observations along the AE and BF axes were strategically placed to unveil features aligned with the typical orientation of BLCLs. This design approach also aimed to optimize the utilization of the current operational observing network (Fig. 5). Sites A, B, D, and E were strategically situated at operational Automated Weather Stations (AWSs) located in Dengkou, Bayin Engel, Yihewusu, and Linhe, respectively, while site F was situated near the sole operational AWS, Habailaigeng, within the desert interior.

d. Instruments and their deployment. In conjunction with the operational observational network (as depicted in Fig. 5), supplementary instruments were deployed to monitor various aspects of land surface conditions, PBL processes, CI, and the following convective organization

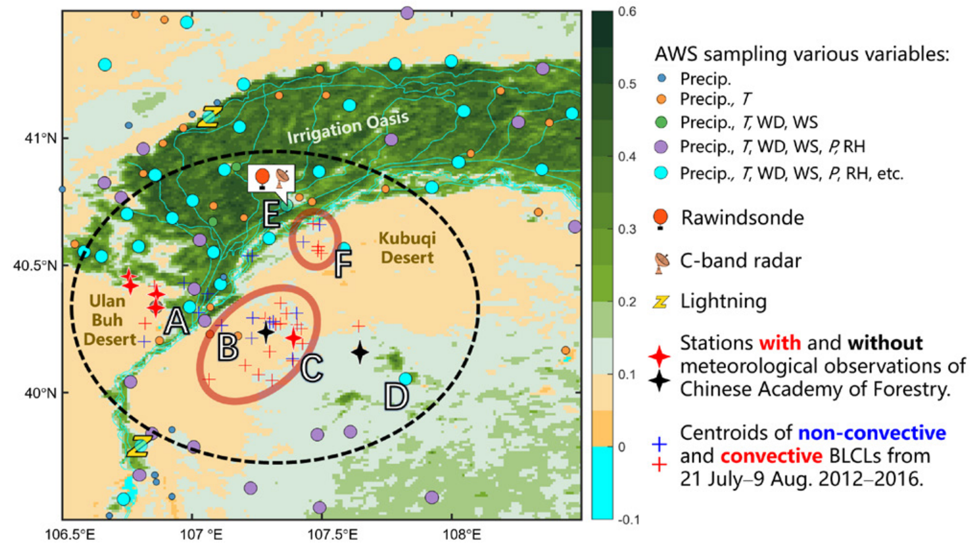

Fig. 5. Distribution of the current observational network and the centroids of nonconvective (blue crosses) and convective (red crosses) BLCLs from 21 Jul to 9 Aug during 2012–16. The shading denotes EVI. The Yellow River and irrigation canals are denoted by cyan curves. Capital letters A–F denote the observation sites of DECODE.

(as outlined in Table 1). These instruments encompassed a range of technologies, including soil temperature and moisture sensors, eddy covariance systems, portable radiosondes,[1] Doppler lidars, microwave radiometers, portable AWS, and a C-band polarimetric Doppler radar. Additionally, support was enlisted for aircraft observations and access to super rapid scan satellite data.

In Fig. 4, soil temperature and moisture sensors were strategically installed at sites A, B, D, and E to capture the spatial variability in soil temperature and moisture within the DECODE domain. At sites A and B, eddy covariance systems were deployed to monitor the diurnal variation in heat, momentum, and moisture fluxes across desert and oasis regions and their differences. Oasis sites A and E, along with desert sites B and F, were equipped with a suite of instruments including microwave radiometers, Doppler lidars, portable radiosondes, and operational AWSs. These instruments facilitated the measurement of diurnal variations in temperature, moisture, and wind across desert and oasis contrast, delineating

[1] The radiosondes employed at DECODE sites were produced by the Nanjing University of Information Science and Technology (NUIST), China (Han et al. 2017; Zhu et al. 2018). It uses a balloon with a diameter of 50 cm filled with helium, with best accuracy below 5 km AGL. The observation error below 5 km AGL is less than 0.3 K for temperature, 0.5 hPa for pressure, 4% for relative humidity, 5° for wind direction, and 0.5 m s^{-1} for wind speed.

Table 1. Special instruments deployed in the field campaign and observing targets.

Instruments	Observing time	Location	Observing targets				
			Land surface	PBL processes	BLCL evolution	Convection initiation	Convection organization
Soil T and RH sensors	Continuous	Sites A, B, E, D	√		√		
Eddy covariance system	Continuous	Sites A, B		√			
Radiosonde	Upon necessity	Portable		√	√	√	√
Doppler lidar	Continuous	Sites A, B, E, F		√	√	√	
Microwave radiometer	Continuous	Sites A, B, E, F		√	√	√	
C-POL radar	Continuous	Site D			√	√	√
Portable AWS	Continuous	Site C		√	√	√	√
Aircraft DMT system	18 Jul; 4 Aug; 9 Aug	DECODE region				√	√
FY-4B satellite	Continuous	DECODE region			√	√	√

their differences. Moreover, they provided insights into the vertical structures of BLCLs and associated thermal circulations, as well as interactions among various PBL processes.

Throughout the 36-day field campaign, a total of 725 radiosondes were successfully launched in key regions, with time intervals ranging from 30 min to 3 h. These launches captured vertical profiles of wind, humidity, and temperature within the PBL both before and after the formation of BLCLs and their associated convection. During the pilot experiment period, radiosondes were launched every 3 h for 1 week at the six sites to capture the diurnal variations in boundary layer characteristics across contrasting vegetation types. In addition to the radiosondes launched by the project team, 43 operational radiosondes were added at 1400 LST at Ejina, Bayannurgong, and Dongsheng. This supplement was conducted alongside the standard operations at 0800 and 2000 LST, aimed at gathering environmental characteristics in both upstream and downstream areas of the field domain.

To effectively monitor BLCLs and their associated convection initiation and organization, downstream site D was equipped with the C-band polarimetric Doppler radar from Nanjing University (NJU C-POL), complementing the operational C-band Doppler radar stationed at oasis site E. The operational radar at site E operated in PPI mode (VCP21), scanning at nine elevations every 6 min. Positioned about 70 km apart from site E, the NJU C-POL radar at site D primarily operated in PPI mode and transitioned to RHI mode in necessity. Observations from both radars facilitated the retrieval of wind fields. These retrieved winds, coupled with the reflectivity, radial velocity, and polarimetric radar variables, provided valuable dataset to understand the formation of BLCLs, CI processes, and the subsequent upscale growth, structure, and propagation of convection.

Supported by the Inner Mongolia Weather Modification Center, aircrafts were deployed from Huhhot Airport, about 300 km away from the operational domain, during three separate events. The aircraft was equipped with instruments from Droplet Measurement Technologies (DMTs), enabling the capture of temperature, pressure, dynamic pressure, humidity, three-dimensional wind, as well as cloud, aerosol, and precipitation particle concentrations and size distributions within the range of 0.1–6200 μm at an altitude of ~3 km AGL. Each flight lasted 1.5 h in the DECODE domain targeting BLCLs.

DECODE also benefited significantly from support provided by the National Satellite Meteorological Center of China (NSMC). For 32 out of 36-day field phase, the *FY-4B* Geostationary High-Speed Imager (GHI) satellite from the NSMC covered the DECODE domain, delivering real-time animations of super rapid scan imagery at 1-min intervals with a horizontal resolution of 250 m at nadir, which is available at the NSMC website (https://satellite.nsmc.org.cn/metafy/en/). These satellite data proved instrumental in capturing the evolution of BLCLs and CI from a cloud perspective (Purdom 1976) and thus played a crucial role in planning field radiosonde operations.

e. Implementation of the campaign. The field campaign was conducted by a team of ~100 participants, comprising 39 observers (Fig. 6a), 20 technical support personnel, and 30 logistic support personnel hailing from 23 agencies and universities across China. In particular, 20 students were involved in the project, with 17 actively participating in onsite observations, playing active roles in designing, preparing, and executing the field experiment. Each team at the six sites comprised a mix of research faculties, operational forecasters, and students from various universities, fostering a seamless integration of research and operational expertise. This provided students with invaluable hands-on experience in applying theoretical knowledge to practical weather forecasting.

The operation center was established at site A, where the steering group orchestrated the experiment through morning meetings and afternoon weather discussions. Daily morning meetings convened online at 0800 LST, providing a platform for reporting the status of

Fig. 6. **Pictures of (a) part of the onsite team and (b),(c) examples of onsite training courses.**

observations and equipment. These meetings were pivotal for issuing specific observation strategies for the day, informed by weather discussions held the previous day. At 1600 LST, daily weather discussions were conducted, offering a comprehensive review of the activities surrounding BLCLs and CI from the preceding day. During these discussions, model predictions were scrutinized, focusing on evaluating forecasts for various scale processes anticipated for the following day. Importantly, this session culminated in the determination of the observation strategy for the ensuing day.

Forecasting played an integral role in both the planning and execution of DECODE. An 18-h forecast spanning from 0200 to 0800 LST of the following day was generated utilizing two regional models. The WRF-ARW model, featuring an innermost domain covering the intensive observation region with a grid spacing of 1 km and a time resolution of 10 min, provided deterministic forecasts for the occurrences of BLCLs and CI. Initial and boundary conditions for this model were derived from GFS forecasts, featuring a horizontal grid spacing of 0.25° × 0.25° and a 3-h time interval. For DECODE operations, WRF forecasts were promptly issued daily at 1500 LST on day 1, covering a valid time window from 0800 to 2000 LST on day 2 (integrating over 6–18 h). The second model employed was the operational Rapid-Refresh Multiscale Analysis and Prediction System (RMAPS-NM), featuring a 3-km grid spacing in the innermost domain. Forecast radiosondes at the six sites were taken from GFS forecasts, providing insights into the potential for convection based on derived parameters such as CAPE, shear, storm-relative helicity, and others.

At the end of the daily weather discussions, forecasts from aforementioned three sources were utilized to determine the observation strategies. On days when observation targets were predicted for the following day, decisions were made regarding the deployment of radiosondes, considering whether they would be deployed in a fixed or mobile manner, along with specifying the detailed time and locations of deployment. Additionally, determinations were made regarding the potential deployment of aircraft, including specifying flight paths and potential takeoff times.

During periods between significant weather events, a total of 16 short courses were conducted (Figs. 6b,c), including seven times of literature reviews, with 5 of them presented by onsite students, six times of introductions on DECODE-related mesoscale processes and advanced instruments, and three times of research methods.

4. BLCLs and associated deep convection

a. BLCL overview. Despite the challenges posed by the COVID-19 pandemic and the inherent difficulties in conducting observations over uninhabited desert areas, the field campaign emerged as a huge success. Over the course of the 36-day experiment, the team encountered 29 BLCLs (Figs. 7 and 8a), along with 66 gust fronts, 12 horizontal convective rolls (HCRs; linear bands of enhanced radar reflectivity factor with a much larger along-wind extent than crosswind extent (Banghoff et al. 2020; Stensrud et al. 2022), multiple supercells, and even one tornado. Sixteen out of 29 BLCLs initiated deep convection. Following the methodology outlined by Huang et al. (2019), BLCLs were identified as linear areas of enhanced reflectivity characterized by a width of less than 10 km, a length greater than 10 km, and a duration of at least 6 min (Wilson and Schreiber 1986) based on the vertical maximum reflectivity of the two lowest elevations of 0.5° and 1.5°. Notably, 18 out of 29 BLCLs occurred between 21 July and 9 August, surpassing the statistical frequency observed from 2012 to 2016 (~9 per year).

Out of the 29 BLCLs observed, 24 formed along the border between the oasis and the Kubuqi Desert (Fig. 8a). Only five BLCLs occurred along the border between the oasis and the Ulan Buh Desert. All BLCLs featured a dominant orientation along the border between the oasis and the desert, with the centroid predominantly appearing in the observation domain in the southwest part of the Kubuqi Desert. A unique dataset was collected on radar fine lines of these BLCLs, showcasing various morphologies in terms of curvatures (Figs. 8b,d,e), length, aspect ratio (Fig. 8c), locations relative to and distances from the desert–oasis border (Figs. 8b,d,f), etc. All these morphologies had been noticed in our statistical analyses for the years 2012–16. Some changes in the morphologies of BLCLs were found to result from their interactions with gust fronts and HCRs (Fig. 8f).

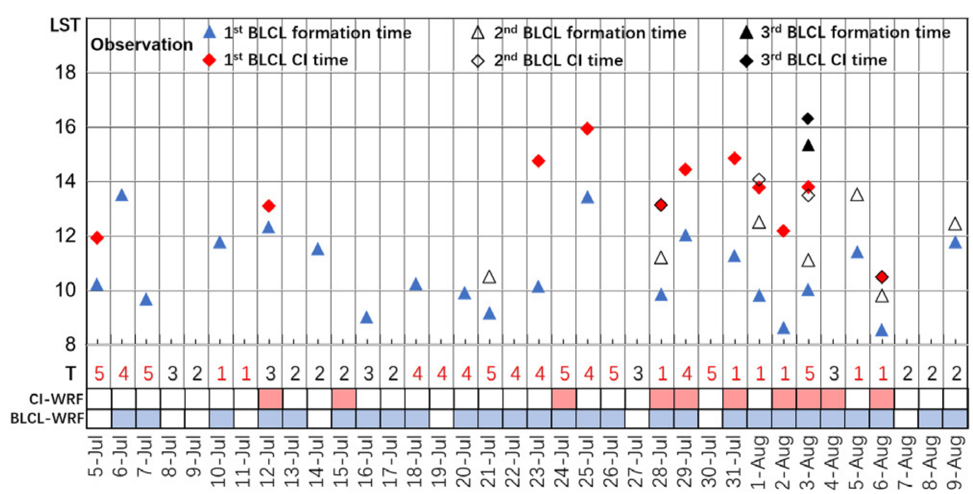

Fig. 7. Temporal distribution of the observed BLCL formation times (triangles), along with the CI times of the convective BLCLs, denoted by diamonds. The serial numbers of BLCLs on each day are represented as first, second, third, and so forth. Synoptic patterns observed are represented by numbers labeled by T on the *y* axis, with T1, T4, and T5 highlighted in red to signify favorable patterns. At the bottom of the graph, WRF-forecasted BLCL days are marked with blue squares, while BLCL-associated CI days are denoted by red squares.

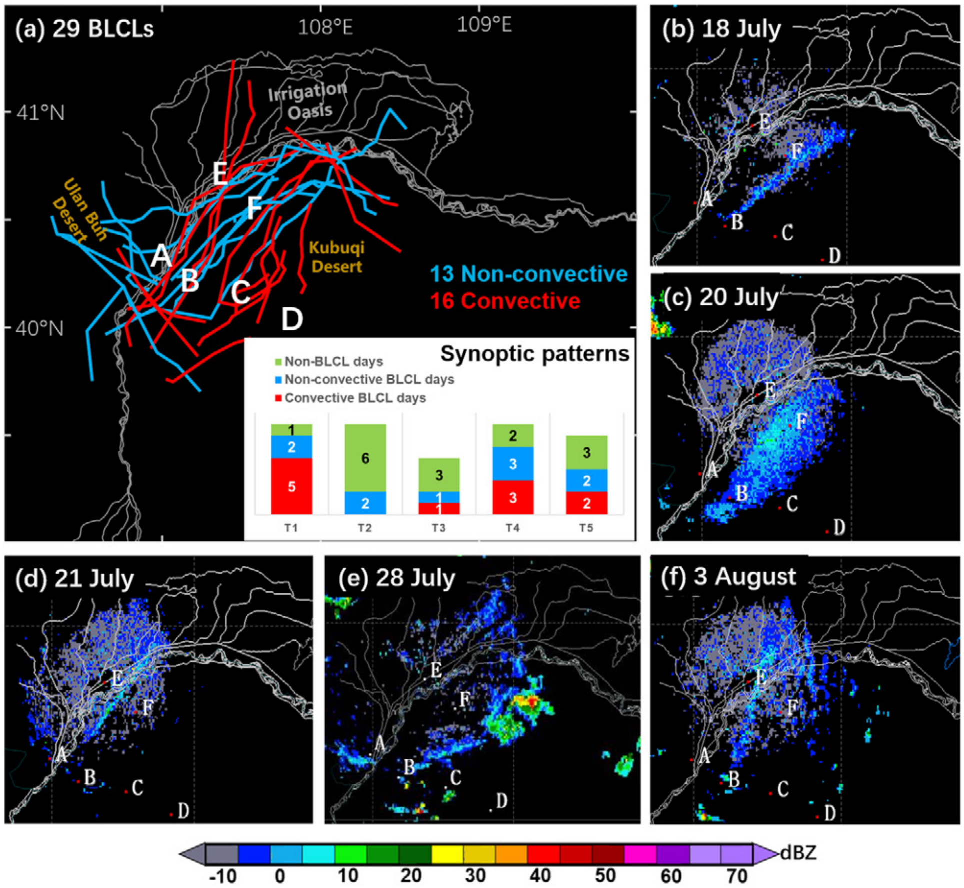

Fig. 8. **(a) Spatial distribution of observed BLCLs and (b)–(f) examples of observed BLCLs and their associated convection during DECODE. The inset panel of (a) illustrates the frequency of convective BLCLs, nonconvective BLCLs, and days without BLCLs across different synoptic patterns. Capital letters A–F denote DECODE observation sites. The gray background contours denote the Yellow River and irrigation canals.**

b. The first multi-observational platform view of a BLCL. On 18 July 2022, a BLCL began to manifest as a fine line on radar reflectivity at 1044 LST, emerging between sites E and F and rapidly extending to the region between sites A and B at 1515 LST (Fig. 9a). It persisted approximately along the BF axis for nearly 10 h within the synoptic pattern T4, which is highly conducive to BLCL formation. This event provided inaugural opportunity to capture the multiple observational platform view of the BLCL through ground photography (Fig. 9b), aircraft imagery at 3 km AGL (Fig. 9c), and remote sensing from satellite (Fig. 9d) and radar (Fig. 9a), all obtained at approximately the same time around 1500 LST.

c. Model verification. Despite perceptible and varied forecast errors in time and location, our real-time forecasts by the 1-km WRF Model decently predicted the occurrence of BLCLs on 19 out of 21 BLCL days (Fig. 7). These forecasts yielded an equitable threat score (ETS) of 0.25 and a bias score (BS) of 1.29, suggesting slight overestimation. ETS and BS (Wilks 1995; Jolliffe and Stephenson 2003; Zhang and Meng 2019) are defined as

$$\mathrm{ETS} = (H - R)/(H + M + \mathrm{FA} - R), \tag{1}$$

$$R = (H + M) \times (H + \mathrm{FA})/N, \tag{2}$$

$$\mathrm{BS} = (H + \mathrm{FA})/(H + M), \tag{3}$$

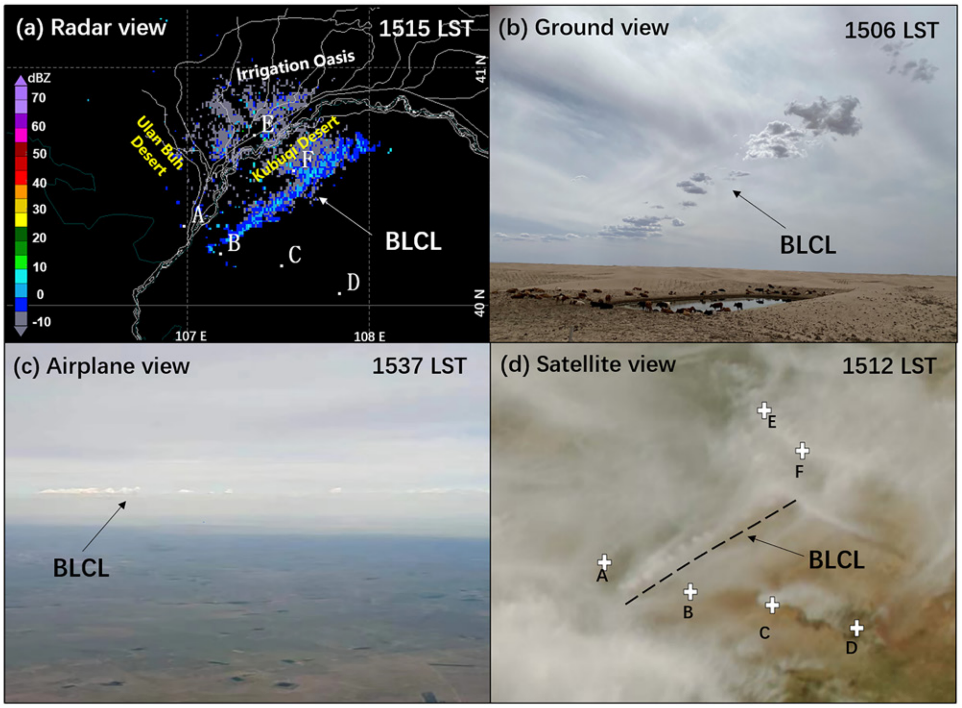

Fig. 9. Multiobservational platform view of the BLCL at approximately 1500 LST 18 Jul 2022. The gray background contours in (a) denote the Yellow River and irrigation canals.

where H, M, and FA are the number of hits (observed and predicted), misses (observed but not predicted), and false alarms (predicted but not observed) days, respectively, among all verification days N. The ETS is the fraction of correctly predicted observed events excluding random hits. A perfect ETS is 1.0, while $-1/3$ is the lower limit and 0 is the threshold for no skill. The BS is the ratio between predicted and observed events, with 1 as the threshold for over (>1) and under (<1) prediction. Additionally, the forecasts accurately predicted the occurrence of BLCL-associated CI on 7 out of 11 days, yielding an ETS of 0.36 and a bias score of 0.91, suggesting slight underestimation.

d. Synoptic patterns. During the field phase of DECODE, the synoptic environmental conditions proved to be highly conducive. Out of the total 36-day observation period, 23 days were favorable, comprising eight instances of T1, 8 of T4, and 7 of T5 patterns (Figs. 7 and 8a). This percentage, ~64%, exceeded the average percentage of 58% observed from 2012 to 2016. In the period from 21 July to 9 August, when the highest frequency of BLCL occurred (Fig. 2c), only 5 days were deemed unfavorable in 2022 (Fig. 7). Consistent with the statistics, T1 predominated in 2022 (Fig. 8a). Among the 29 observed BLCLs, 24 (83%) BLCLs with 15 (94%) convective BLCLs occurred within these three favorable patterns, further confirming the robustness of the synoptic pattern classification. Both the WRF and RMAPS-NM models were capable of reasonably capturing the appropriate synoptic patterns, thereby proving invaluable in planning intensive observation or anticipating downtimes.

e. Land surface and PBL features across the desert–oasis contrast. Using site E as a representative oasis site[2] and site B as a representative desert site, we compared the diurnal cycle of soil temperature and relative humidity at a depth of −10 cm (T_{-10}, RH_{-10}) across the desert–oasis contrast averaged over the entire field phase. It was observed that T_{-10} at site E

[2] The ground of AWS at site A was under construction and thus less representative of oasis relative to site E. The eddy covariance system was installed in the outfield rather than at the AWS station and thus was representative.

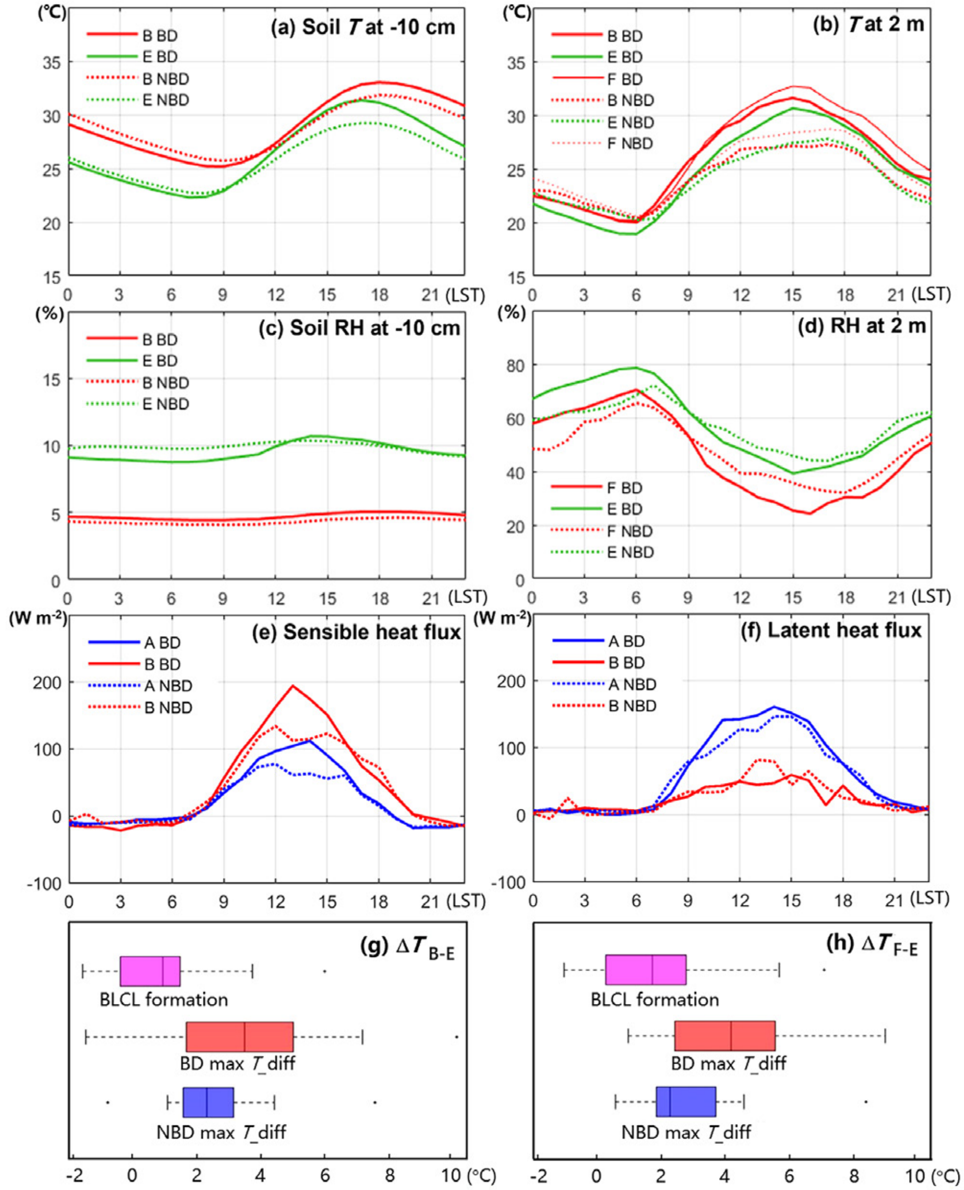

Fig. 10. Averaged diurnal variations of (a) T_{-10} (°C) and (c) RH_{-10} (%) for sites B (desert) and E (oasis), (b) T_2 (°C) for sites B (desert), E (oasis), and F (desert), (d) RH_2 (%) for sites E (oasis) and F (desert), alongside (e) sensible heat flux (W m^{-2}) and (f) latent heat flux (W m^{-2}) for sites A (oasis) and B (desert). The labels "BD" denote the average over BLCL days, while "NBD" signifies the average over non-BLCL days. (g),(h) Box-and-whisker diagrams depicting the T_2 differences between sites B (desert) and E (oasis) as well as between sites F (desert) and E (oasis) at BLCL formation time and the time when maximum difference in T_2 at day time occurred on BLCL (BD) and non-BLCL (NBD) days. The percentile extents and corresponding values represent the 25th–75th percentiles for boxes, with the 10th–90th percentiles for whiskers and the 50th percentiles for the lines in boxes. Outliers blow the 10th percentile and exceeding the 90th percentile are shown in blue dots.

consistently registered lower values compared to those at site B, exhibiting an earlier maximum and minimum by ~1 h (Fig. 10a). On days featuring BLCLs (denoted by BD), the maxima of T_{-10} at sites E and B were higher than those on non-BLCL days (denoted by NBD) by ~3°C, with a more pronounced difference observed at the oasis site E. The RH_{-10} at the oasis site E were higher by 5% than at the desert site B (Fig. 10c) on both BD and NBD. Unlike T_{-10}, RH_{-10} at both sites did not exhibit apparent diurnal variation or apparent differences between BD and NBD.

The maxima and minima of diurnal cycles of 2-m air temperature (T_2) appeared slightly earlier than those of average T_{-10} at both sites B and E (Fig. 10b). On BLCL days, the oasis site E exhibited a maximum T_2 of ~31°C, which was ~1.5°C lower than that at the desert site B, possibly due to evaporative cooling. The maximum T_2 at sites B and E on non-BLCL days was lower than their counterparts on BLCL days by 4°–5°C, exhibiting smaller differences between sites B and E than on BLCL days. The median of the maximum difference in T_2 between sites B and E was 3.5°C (Fig. 10g) on BLCL days, ~1.5°C higher than that on non-BLCL days. However, the median of the difference in T_2 at the BLCL formation time was only 1°C. The real-time WRF forecast tended to overpredict maximum T_2 by ~2°C on BLCL days and ~3°C on non-BLCL days, potentially leading to the overestimation of BLCL formation.

Differences in T_2 between the pure desert site F and oasis site E were apparently higher than those between B and E. The maximum T_2 at site F was 3°C higher than that at site E (Fig. 10b), which was almost twice the difference in maximum T_2 between B and E. The median of the maximum difference in T_2 between F and E on BLCL days was 4.2°C, with the highest difference of 9°C (Fig. 10h). These magnitudes were much higher than those due to contrast between irrigated and nonirrigated grassland documented in GRAINEX (0.6°C; Lachenmeier et al. 2024), LIAISE (2.8°C; Brooke et al. 2024), and observed climatological dataset (1.018°C; Mahmood et al. 2004, 2006, 2013). These larger contrast in T_2 between oasis and desert could be why the thermal circulation and BLCL signal are more persistent in the study area and cause CI in DECODE than other irrigation contrast regions. The 2-m air relative humidity (RH_2) exhibited a higher magnitude at oasis site E than at desert site F by ~10% in the entire diurnal cycle on both BLCL and non-BLCL days (Fig. 10d). The minimum RH_2 was observed at the time of maximum T_2, with a lower magnitude on BLCL days compared to non-BLCL days by 5%–10%.

Flux observations at sites A and B showed notable differences between oasis and desert environments. At oasis site A, the maximum of diurnal cycles of the average sensible heat flux was lower than that of the latent heat flux, whereas the opposite trend was observed at the desert site B (Figs. 10e,f). Site A exhibited a higher latent heat flux and a lower sensible heat flux compared to site B, with larger disparities between the two sites observed on BLCL days compared to non-BLCL days. On BLCL days, likely due to higher soil temperature and T_2, sensible heat fluxes at both sites A and B were higher than on non-BLCL days. Latent heat flux exhibited less changes between BLCL days and non-BLCL days. The magnitudes of the sensible heat fluxes at noon on non-BLCL days at A and B are similar to those at irrigated and nonirrigated areas observed in July 2018 in southeastern Nebraska, the United States (Rappin et al. 2021).

As expected, the median surface wind speed at site B at the time of maximum difference in T_2 on BLCL days was ~3 m s^{-1}, slightly weaker compared to non-BLCL days (Fig. 11a), which is consistent with previous findings that thermal circulation induced by land heterogeneity is preferred under the conditions of a weak background wind (Segal and Arritt 1992; Mahrt et al. 1994; Lee et al. 2019). On the contrary, the median surface wind speed at site E at the time of maximum difference in T_2 on BLCL days was slightly stronger than on non-BLCL days (Fig. 11b), possibly owning to the occurrence of oasis breeze. Both sites exhibited a smaller median wind speed at BLCL formation time than at the time of maximum difference in T_2. Winds at the oasis site E were all weaker than winds at the desert site B in all the three situations.

Shifts in the wind direction over time were consistent with BLCL initiation. From early morning to early afternoon on BLCL days, the near-surface wind at the oasis site E, as indicated by the median wind direction in the 90 degree extent (from 0° to 360°) with the highest frequency of occurrence, shifted from easterly to northerly (Fig. 11c). This shift was probably due to the occurrence of oasis breeze. Meanwhile, winds at desert site B on BLCL days were predominantly southerly, generally opposing the oasis breeze (Fig. 11d). The resulting convergence between E and B was favorable for BLCL initiation. Conversely, on non-BLCL days,

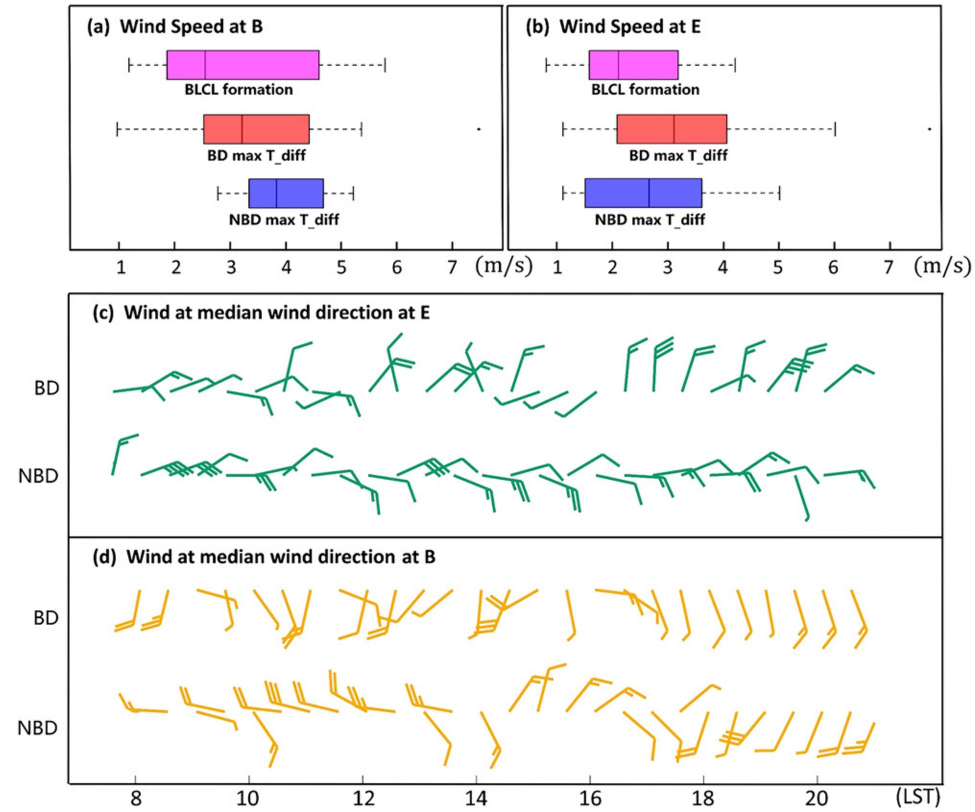

Fig. 11. Box-and-whisker diagrams depicting the absolute wind speed at sites (a) B (desert) and (b) E (oasis) at BLCL formation time and the time when maximum difference in T_2 at day time occurred on BLCL (BD) and non-BLCL (NBD) days. The percentile extents and corresponding values represent the 25th–75th percentiles for boxes, with the 10th–90th percentiles for whiskers and the 50th percentiles for the lines in boxes. Outliers blow the 10th percentile and exceeding the 90th percentile are shown in blue dots. (c),(d) The variation of the median wind direction in the 90° extent (from 0° to 360°), with the highest frequency of occurrence on BLCL (BD) and non-BLCL (NBD) days during DECODE, at sites E (oasis) and B (desert). Half barbs and full barbs represent 1 and 2 m s^{-1}, respectively.

the near-surface winds from early morning to early afternoon were predominantly easterly at site E and westerly or northerly at site B, exhibiting no apparent convergence.

f. Desert–oasis thermal circulations. A BLCL in this work signifies the convergence associated with the updraft branch of a thermal circulation generated by the contrast between the desert and oasis environments. Uniquely, DECODE captured full thermal circulations across desert–oasis boundary through dual-Doppler wind retrieval and simultaneous radiosonde measurements, which completed previous observational evidence of thermal circulations.

Through dual-Doppler retrieval, updraft branches of thermal circulations were captured. For example, on 20 July 2022, a BLCL emerged at 0955 LST over the desert, exhibiting a radar reflectivity pattern with the above average aspect ratio oriented along the BF axes at 1544 LST, as observed by both the LHRD at site E (Fig. 12a) and the NJU C-POL radar at site D (Fig. 12d). The expansive radar reflectivity pattern manifested as a zone of clouds along the border between the oasis and the Kubuqi Desert (Fig. 12g). Radial velocities from both radars revealed a distinct convergence line between inbound and outbound radial velocities, approximately aligned along the major axis of the reflectivity pattern (Figs. 12b,e). The extensive radar echoes facilitated the execution of dual-Doppler wind retrieval, enabling the capture of the desert segment of the thermal circulation (Fig. 12h). The thermal circulation displayed evident convergence from the ground to ~1.5 km AGL (Figs. 12h,f,i) and apparent divergence above 2 km AGL (Figs. 12f,c).

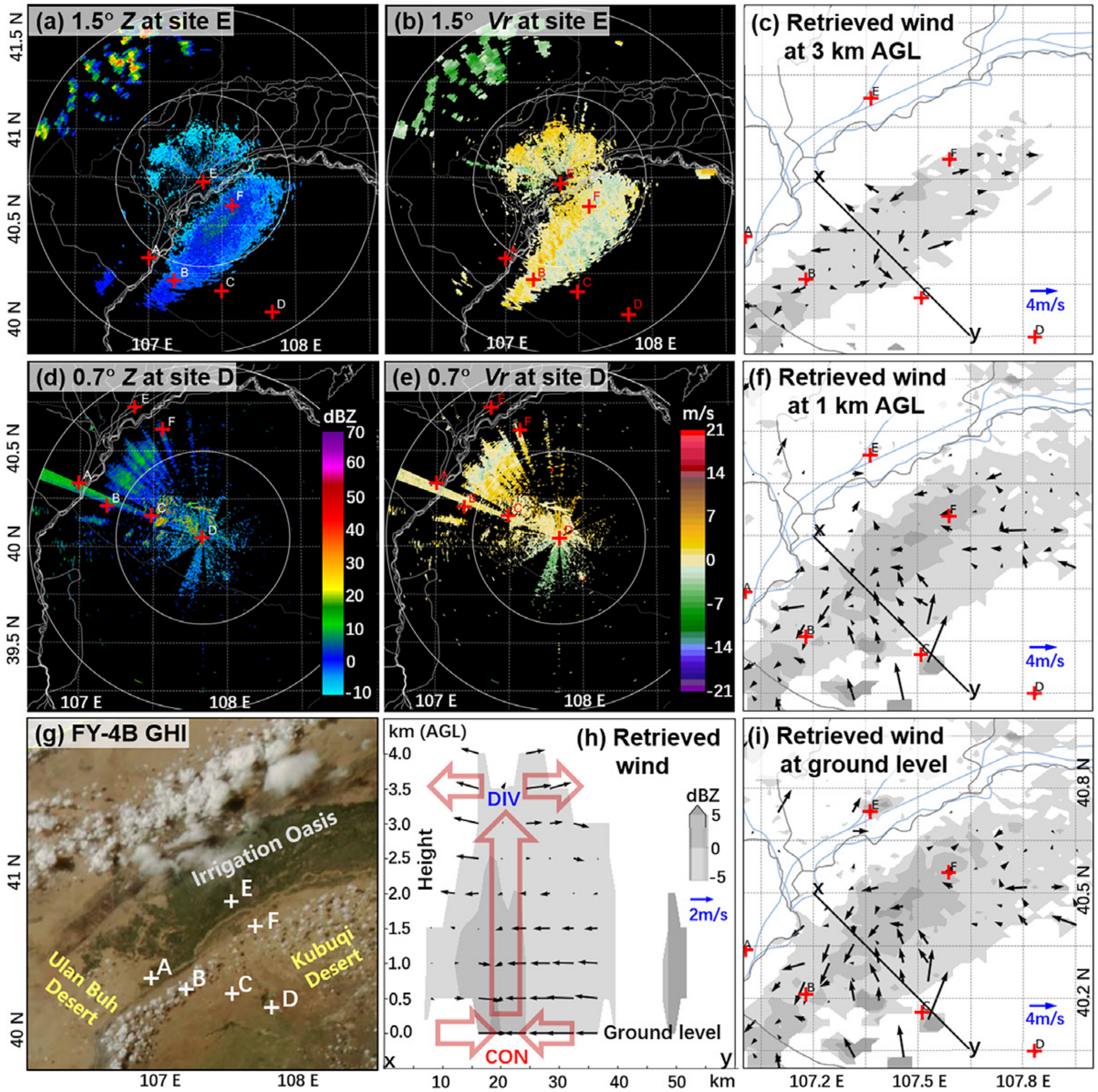

Fig. 12. Features of the BLCL on 20 Jul 2022, which was unique in terms of the radar reflectivity pattern of an above average aspect ratio, including (a) radar reflectivity *Z* and (b) radial velocity *Vr* at 1.5° elevation from the LHRD at site E at 1544 LST 20 Jul 2022. (d),(e) As in (a) and (b), but from the NJU C-POL radar at site D at 0.7° elevation at 1546 LST. (g) The *FY-4B* GHI satellite image at 1546 LST. Dual-Doppler wind retrievals are depicted horizontally at 1544 LST at (c) 3 km AGL, (f) 1 km AGL, (i) ground level, and (h) vertically along the line from "x" to "y" as marked in (c), (f), and (i). The shading in (h), (c), (f), and (i) represents the reflectivity observed by the LHRD. The maroon empty arrows in (h) highlight the updraft branch of the thermal circulation. "DIV" and "CON" denote divergence and convergence, respectively. The crosses in (a)–(f), (g), and (i) indicate the six sites from A to E. The gray background contours in (a)–(f) and (i) denote the Yellow River and irrigation canals.

In two instances of convective BLCL events, full thermal circulations were probed using simultaneously launched radiosondes strategically distributed perpendicular to the BLCLs. For example, on 31 July 2022, a BLCL formed within a synoptic pattern T5, known for its propensity to favor convective BLCLs, almost precisely positioned over the desert–oasis boundary and perpendicular to the HCR (Figs. 13a,c–e). The thermal circulation was captured by radiosondes launched simultaneously from six spots perpendicular to the BLCL every 30 min. The vertical profiles of wind and virtual potential temperature anomalies from background wind profiles averaged over these six spots following Rochetin et al. (2017) are shown in Fig. 13b.

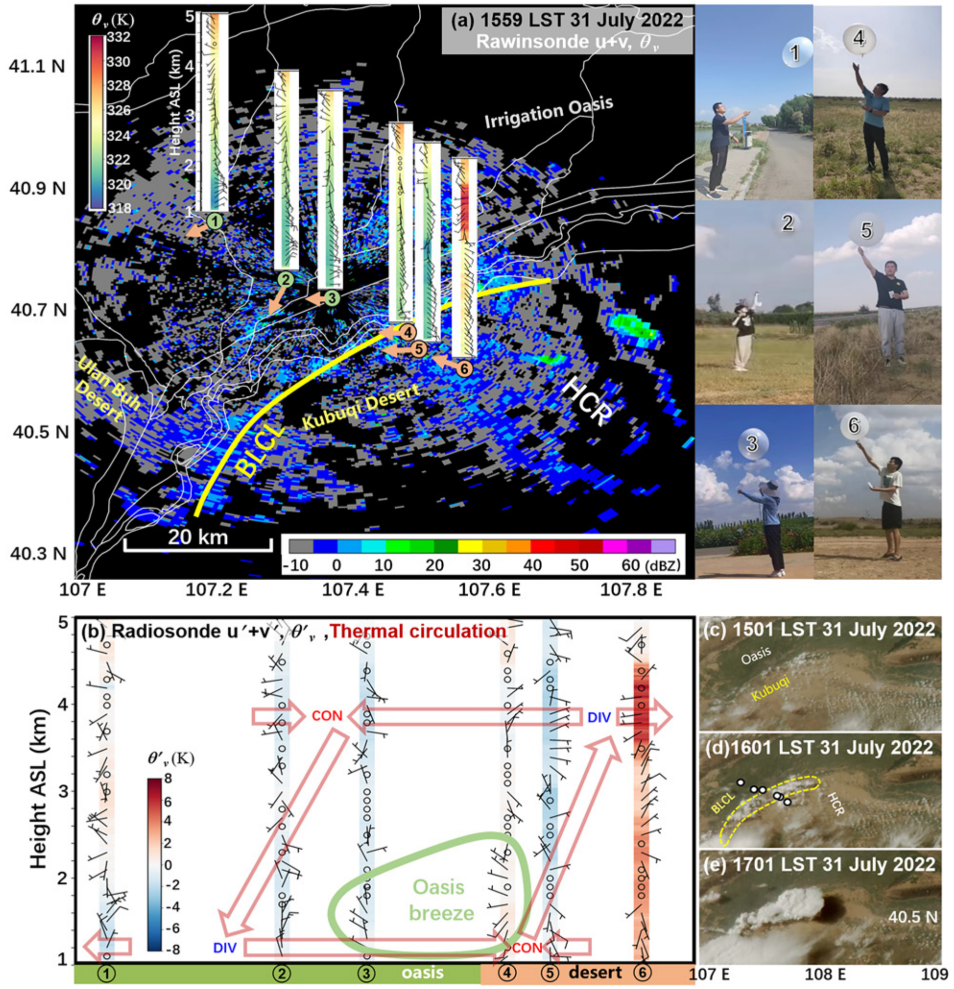

Fig. 13. (a) Simultaneous radiosonde deployment at six spots numbered 1–6 at 1559 LST 31 Jul 2022 from 1 to 5 km MSL in the background of radar reflectivity at 1.5° elevation of LHRD at the same time. The virtual potential temperature (θ_v; K) is given in shading in each white column. The heavy brown arrow denotes near-surface wind at the six radiosondes numbered in green (for oasis sites) and brown (for desert sites) dots. The yellow line denotes the BLCL. The half barbs and full barbs represent 2 and 4 m s^{-1}, respectively. The gray background contour denotes the Yellow River and irrigation canals. The pictures with numbered balloons correspond to the six radiosondes. (b) Profiles of wind and virtual potential temperature anomalies θ_v' with respect to the mean background profile along the six radiosonde locations. The green shading along the *x* axis denotes oasis, and the brown shading denotes desert. The maroon empty arrows indicate the thermal circulation, which extended to ~3 km in depth. DIV and CON denote divergence and convergence, respectively. (c)–(e) The *FY-4B* GHI satellite images at 1501, 1601, and 1701 LST. The dashed yellow contour in (d) denotes the cloud line of the BLCL. The white dots denote the six radiosonde locations.

Figure 13b depicts a convergence over the desert side between spots 3, 4, and 5 near the surface overlapped with apparent divergence at ~4 km MSL (3 km AGL) and a divergence over the oasis side between spots 1 and 2 near the surface overlapped with convergence, with oasis breeze from spots 3 to 4 up to ~2.5 km MSL (1.5 km AGL). This thermal circulation exhibited a width of about 25 km near the surface in terms of the distance between the divergence and convergence centers, and a depth of 3 km. The convergence between spots 4 and 5 extended from the ground to ~3 km MSL (2 km AGL), which was consistent with findings revealed by dual-Doppler wind retrieval for the case on 20 July 2022 (Fig. 12h).

Drawing upon observations from multiple platforms including radar, Doppler lidar, satellite, and radiosondes, ongoing analyses are underway to comprehend the characteristics of different manifestations of the updraft branch of the thermal circulation, including the cloud line observed on visible satellite imagery, the fine line seen on radar reflectivity imagery, and the convergence at the lower section of the updraft branch.

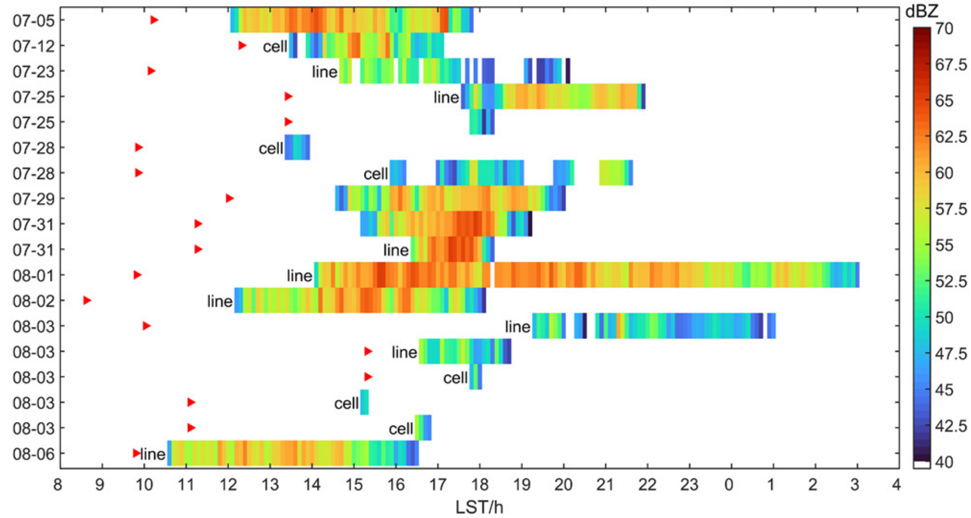

Fig. 14. **Evolution of the maximum reflectivity of the 18 CSs (including eight linear, denoted by "line," and six cellular, denoted by "cell") during their lifespans, as observed by the LHRD at site E. The triangles pointing right indicate the formation time of their parent BLCLs.**

g. BLCL-associated deep convective storms.

1) Overview. Among the 29 observed BLCLs, 16 (55%) initiated convection during the 36-day field campaign (Figs. 7, 8a, 14). This percentage aligned with the average observed from 2012 to 2016, where out of nine BLCLs, 5 were convective (55%) during the period from 21 July to 9 August each year.

CI was determined objectively using the following criteria: 1) a convective cell is identified as a contiguous region with reflectivity of no less than 40 dB*Z* (Parker and Johnson 2000), having a volume of no less than 1 km^3 and a duration of at least 5 min, i.e., lasting at least two continuous volume scans of the LHRD; 2) a convective system (CS) is determined for convective cells situated within a distance of no more than 29 km from each other's edge. The criteria of 29 km yielded results the most consistent with manual identification; 3) a CS whose first 30-dB*Z* reflectivity occurred within 50 km of a BLCL was considered to be initiated by that specific BLCL (Huang et al. 2019). In 0.9–9.3 h following their formation, with an average of 3.9 h, the 16 convective BLCLs initiated a total of 18 CSs, which had an average lifespan of 3.5 h, ranging from 0.1 to 12.7 h within the range of the LHRD (Fig. 14). Among the 18 CSs, eight exhibited linear and six exhibited cellular organizational modes.

2) The golden CI case on 29 July 2022. On 29 July 2022, a CI case occurred, which was regarded as a golden event due to several factors: 1) the BLCL formed over the region in the Kubuqi Desert (Fig. 15a), known from previous studies to have the highest frequency of BLCL formations during the synoptic pattern T4, the most favorable for BLCL formation; 2) the BLCL formed perpendicular to the HCRs, extended into the oasis region, shifted to align with the oasis–desert border over the Kubuqi Desert, and eventually merged with extensive gust fronts (Figs. 15b–i), exhibiting a maximum length of 110 km (Fig. 15a), a width of 10 km, and an altitude of up to 2.6 km AGL (Figs. 15e,k); 3) a series of deep convection were initiated along the BLCL, organizing into an MCS, which produced hails over the oasis region and supercells while propagating eastward over the Kubuqi Desert (Figs. 15e–j); and 4) this event was sampled by all instruments except for the eddy covariance system at site A and aircraft.

Evolutions of the BLCL and oasis breezes were captured by Doppler lidars at the oasis site E and desert site F. When the BLCL passed site E at ~1400 LST (Figs. 16a,b; also Fig. 15a) and site F at ~1530 LST (Figs. 16c,d; also Fig. 15a), the near-surface wind changed

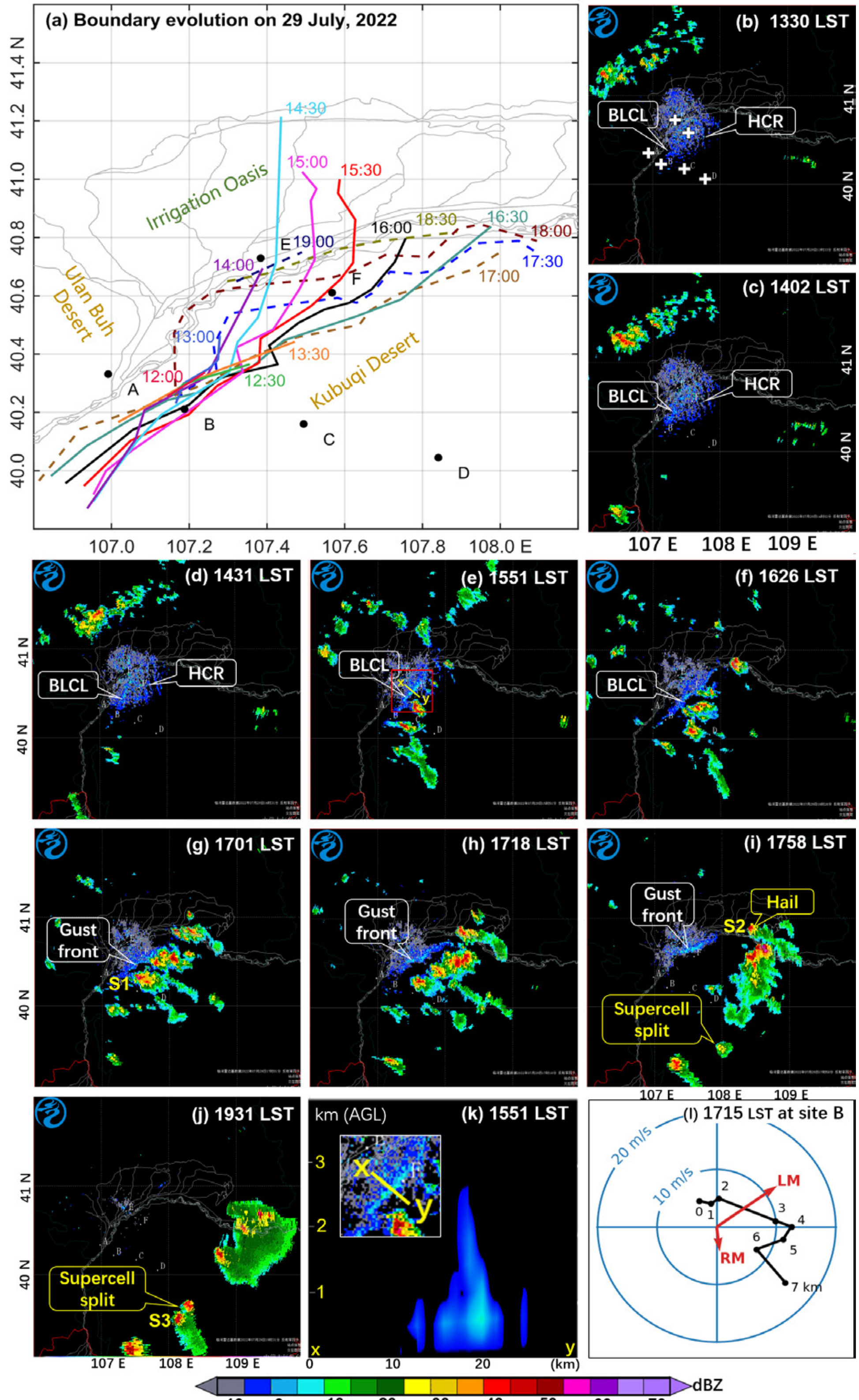

Fig. 15. (a) Evolution of the BLCL (solid color lines) on 29 Jul 2022. The dashed color lines denoted the gust fronts of the generated storms. (b)–(j) Radar reflectivity at 1.5° elevation from the LHRD at site E from 1330 to 1931 LST 29 Jul 2022, showing the evolution of the BLCL relative to the southeast–northwest-orienting HCR (b)–(d), extending into oasis in the northern part (d), then propagating to the Kubuqi Desert region (e), and eventually merging with gust front of the generated storms (f), propagating away from the storms into the oasis region (g)–(i). (d)–(j) The upscale growth of convection, including the development of a splitting supercell (i),(j). S1–S3 denote storms whose microphysics features are shown in Fig. 17. (k) The vertical cross section of radar reflectivity along the short yellow line perpendicular to the BLCL at 1551 LST, with the inset panel zoomed in on the red box highlighted in (e). Hodograph at site B at 1715 LST is given in (l). The gray background contours in (a)–(j) denote the Yellow River and irrigation canals.

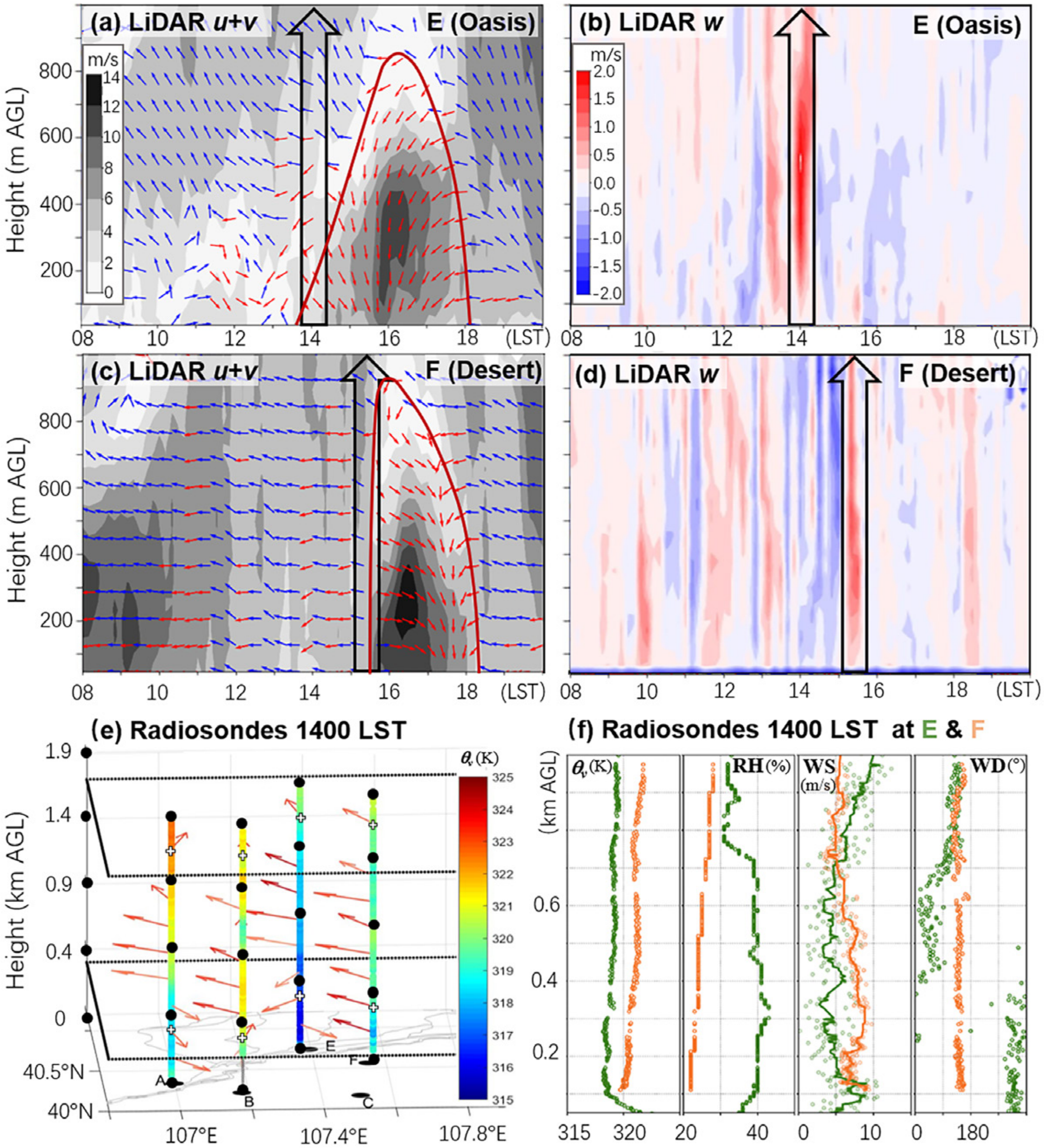

Fig. 16. Evolution of (a),(c) horizontal wind and (b),(d) vertical wind speed observed by Doppler lidars at sites E (oasis) and F (desert), from 0800 to 2000 LST 29 Jul 2022. The maroon contour denotes the oasis breeze coverage. The empty black arrow denotes the time when the BLCL was passing over. The three-dimensional distribution of the horizontal wind and virtual potential temperature (θ_v; K) observed by radiosondes at 1400 LST 29 Jul 2022 at sites A (oasis), B (desert), E (oasis), and F (desert) are provided in (e). The black dots denote the height as labeled in the z axis. The white crosses denote the location of each radiosonde on the two horizontal cross sections. A comparison of θ_v (K), RH (%), wind speed (WS; m s^{-1}), and direction (WD; °) between sites E and F at 1400 LST is given in (f).

from southerly to northerly oasis breeze following the appearance of the maximum vertical wind speed of up to 2 m s^{-1} with a vertical impact range exceeding 1 km (Figs. 16b,d). The northerly oasis breeze extended up to 800 m AGL at sites E and F (Figs. 16a,c) with a maximum horizontal wind speed of ~12 m s^{-1} at ~300-m AGL.

Associated with the updraft branch of the thermal circulation at the BLCL, convergent winds between sites E and F were observed in radiosonde observations at 1400 LST from the ground to ~500 m AGL (Fig. 16e). Site E had a lower wind speed by 5 m s^{-1} at 200 m AGL and opposite wind direction from those at site F (Fig. 16f). Similar convergent wind was also observed between sites A and B (Fig. 16e). The layer above 600 m AGL was predominated by consistent easterly wind. The development of the thermal circulation may be attributed to apparent differences in near-surface temperature and moisture between the oasis site E and desert site F. Radiosondes at sites E and F at 1400 LST exhibited apparently consistent differences in 2-m temperature and relative humidity from the ground to 500 m AGL (Fig. 16f). Relative to site F, site E had a lower temperature by 3°C and a higher relative humidity by 20% at 200 m AGL. The higher relative humidity at the oasis site E than the desert site F might have been contributed by higher evapotranspiration and the convergence near the location of the BLCL.

The BLCL initiated a strong CS along the BLCL starting at 1425 LST (Figs. 15d–j). One storm (S2 in Fig. 15i) generated a 5-mm hail at 1810 LST in the eastern oasis. A supercell developed at the southern end of the CS and underwent a splitting process, resulting in two mirror-symmetric supercells (Figs. 15i,j). Radiosonde at site B at 1715 LST showed an approximately straight hodograph from the ground to 4 km AGL (Fig. 15l), which is favorable for supercell splitting (Klemp 1987).

Microphysical structures of all convective storms in this case, captured by the NJU C-POL located at site D, were examined. These storms exhibited relatively low centroids (Fig. 17a). Below the melting level, the frequency median of the reflectivity factor Z_H decreased toward the ground, whereas the frequency median of the differential reflectivity Z_{DR} increased (Figs. 17a,b). The fingerprint parameter space (Kumjian et al. 2022) of ΔZ_H and ΔZ_{DR} from 4 to 2 km AGL indicated that the collision–coalescence, breakup, and evaporation processes played important roles in precipitation growth (Fig. 17c). In some regions of convection (approximately 28.3%), a balance between coalescence and breakup was observed. Meanwhile, the roles of evaporation and size sorting were also important, contributing 18.8%. Notably, analyses of storms S1–S3 (Figs. 17d–i) illustrated that the prominent reflectivity was predominantly due to hail rather than big raindrops, possibly attributed to the abundant desert dust, which have been found to be active as ice nuclei at temperatures colder than −11°C (Schaefer 1949, 1954) and both ice and condensation nucleating activities of desert dust can enhance the natural ice in the cloud (Rosenfeld and Nirel 1996).

3) Traveling convective systems. BLCLs cannot only initiate pristine convection but may also influence antecedent CSs. This phenomenon was observed twice in the afternoon on 23 and 25 July 2022 during the field phase of DECODE (Fig. 18). Initially, a CS developed west of the oasis (Figs. 18a,d), and a BLCL formed over the Kubuqi Desert along the BF axis. Subsequently, the portion of the CS that traversed the oasis region weakened (denoted by dashed circles in Figs. 18b,e). One possible reason for this weakening could be the impact of the descending branch of the thermal circulation over the oasis. Upon leaving the oasis region, the weakened segment of the CS reinvigorated upon encountering the BLCL, possibly due to the moisture convergence and lifting at the BLCL.

4) A rare tornado case. Tornadoes occurring over desert regions are seldom reported due to limited witnesses. Fortunately, during the DECODE project, three team members chanced upon a tornado (Fig. 19a) while en route to site D at 1619 LST 24 July 2022. As observed by the NJU C-POL radar at site D, the tornado occurred within the hook echo of a supercell (Figs. 19c–e), exhibiting a mesocyclone with a maximum rotational velocity of 16 m s^{-1} and a tornado vortex signature (TVS) with a maximum radial wind difference of 32 m s^{-1} (Fig. 19b). Despite the mesocyclone and TVS persisting for ~ half an hour, the tornado itself lasted only 6 mins.

5. Summary and research opportunities

DECODE stands as a pioneering field campaign dedicated to the study of BLCLs across the desert–oasis contrast and their impact on deep convection initiation and organization.

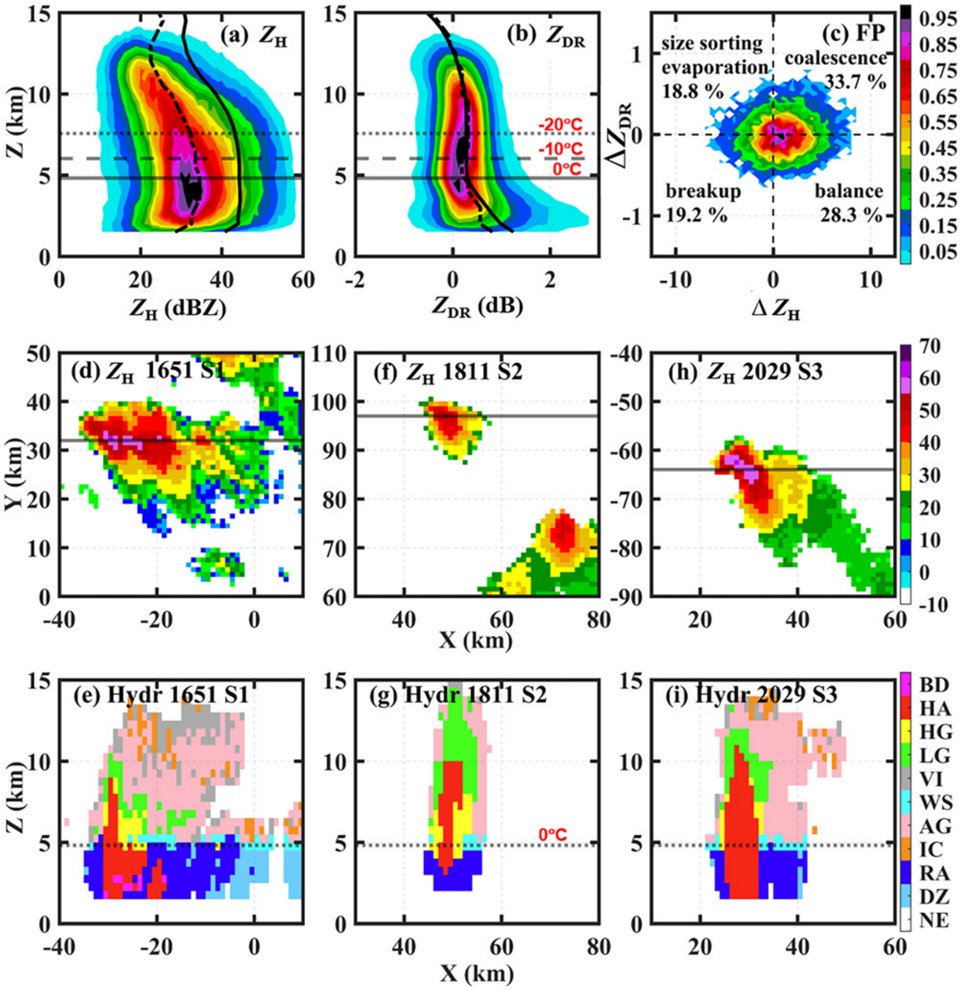

Fig. 17. Microphysical features in the convective regions of all storms that occurred on 29 Jul 2022, captured by the NJU C-POL radar. It includes frequency-by-altitude (MSL) diagrams of (a) Z_H and (b) Z_{DR}, as well as frequency distribution of (c) growth processes of hydrometeors below the melting layer inferred from the vertical gradient in Z_H and Z_{DR} (Δ, with changes from 4 to 2 km MSL; for example, coalescence is inferred by $\Delta Z_H > 0$ and $\Delta Z_{DR} > 0$). The horizontal solid, dashed, and dotted curves in (a) and (b) denote levels of 0°, −10°, and −20°C, respectively. The vertical dashed and solid lines in (a) and (b) denote the median and mean values at different levels, respectively. (d),(f), (h) The Z_H at 3 km MSL and (e),(g),(i) the retrieved hydrometeor types by altitude (MSL) across storm (d),(e) S1 and (f),(g) S2 initiated directly by the BLCL, and (h),(i) the left mover S3 of the split supercell that developed in the downstream propagation of the CS. The three storms have been denoted in Figs. 15g, 15i, 15j. The horizontal dotted lines in (e), (g), and (i) denote levels of 0°C.

From 5 July to 9 August 2022, 29 BLCL events were documented over the desert adjacent to the irrigated oasis in Inner Mongolia, China. Among these, 16 initiated deep convection. Full thermal circulations due to vegetation heterogeneity were captured, completing previous observational evidence mostly revealing partial thermal circulations. These observations were made possible through a comprehensive array of instrumentations, including land surface monitoring, PBL profiling systems such as radiosondes, microwave adiometers, Doppler lidars, and remote sensing facilities such as radars and super rapid scan satellite, as well as aircraft reconnaissance. In addition, a wealth of photographs and time-lapse videos offer a visual view on BLCL formation and its consequential convective processes, and a documentary "Storm Chasing 48 Days" portrays the entire campaign, which are publicly available online (https://opendata.pku.edu.cn/dataverse/DECODE_VIDEO_CATALOG), providing invaluable insights into the instrumental observations of BLCLs and convection dynamics over the desert–oasis interface.

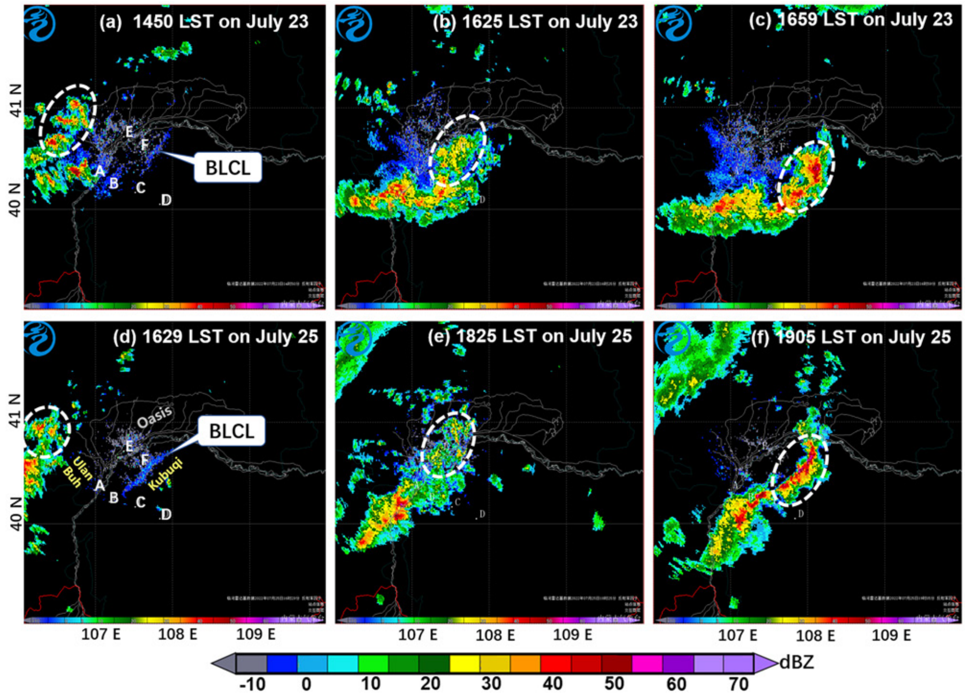

Fig. 18. Evolution of reflectivity at 1.5° elevation of the LHRD when an antecedent CS (denoted by dashed circles) passed over a BLCL on (a)–(c) 23 Jul 2022 and (d)–(f) 25 Jul 2022. Capital letters A–F denote the six sites of DECODE. The gray background contours denote the Yellow River and irrigation canals.

The dataset compiled during DECODE represents an unparalleled resource for advancing our understanding and modeling of land–atmosphere interaction, boundary layer, and convective processes in regions characterized by sharp vegetation gradients. By analyzing the 16 convective and 13 nonconvective BLCLs, as well as 21 BLCL days compared to 15 non-BLCL days, we can delve into the factors influencing convective versus nonconvective BLCLs and distinguish between BLCL and non-BLCL days. The diverse morphologies and locations of the 29 BLCLs provided valuable insights into factors dictating their orientation, curvature, and proximity to the desert–oasis boundary. Moreover, these observations shed light on key features such as PBL height and boundary layer jets over desert and oasis divide (not shown in detail). The impact of irrigation on PBL features especially on the associated BLCL and CI can be examined based on DECODE observations, which will complete our current understanding about the differences mainly in PBL features and convective environments across irrigated and nonirrigated grassland based on campaigns such as GRAINEX (Rappin et al. 2021) and LIAISE (Boone et al. 2021).

Given the real-world BLCL formation and CI across vegetation gradients prove more complex than idealized numerical simulations suggest, beyond the influence of vegetation contrast, factors such as HCRs, gust fronts from antecedent CSs, environmental flow patterns, orography effects, impact of dust aerosol, and their complex interplay warrant thorough investigation. Zhuozi Mountain in the southwestern part of the Kubuqi desert and Lang Mountain west of the oasis may affect the formation of BLCLs and their associated CI through the mountain–valley flow, blocking low-level easterlies or generating gravity wave. A total of 66 gust fronts and 12 HCR events were captured in DECODE. Understanding how BLCLs affect CSs traveling over them remains a key challenge.

The DECODE dataset holds immense potential for model verification and improvement across various aspects, including land–atmosphere interactions, PBL dynamics, impact of irrigation, and microphysical processes. Our preliminary assessments about the performance of WRF Model showed overestimation of surface temperature and underestimation of

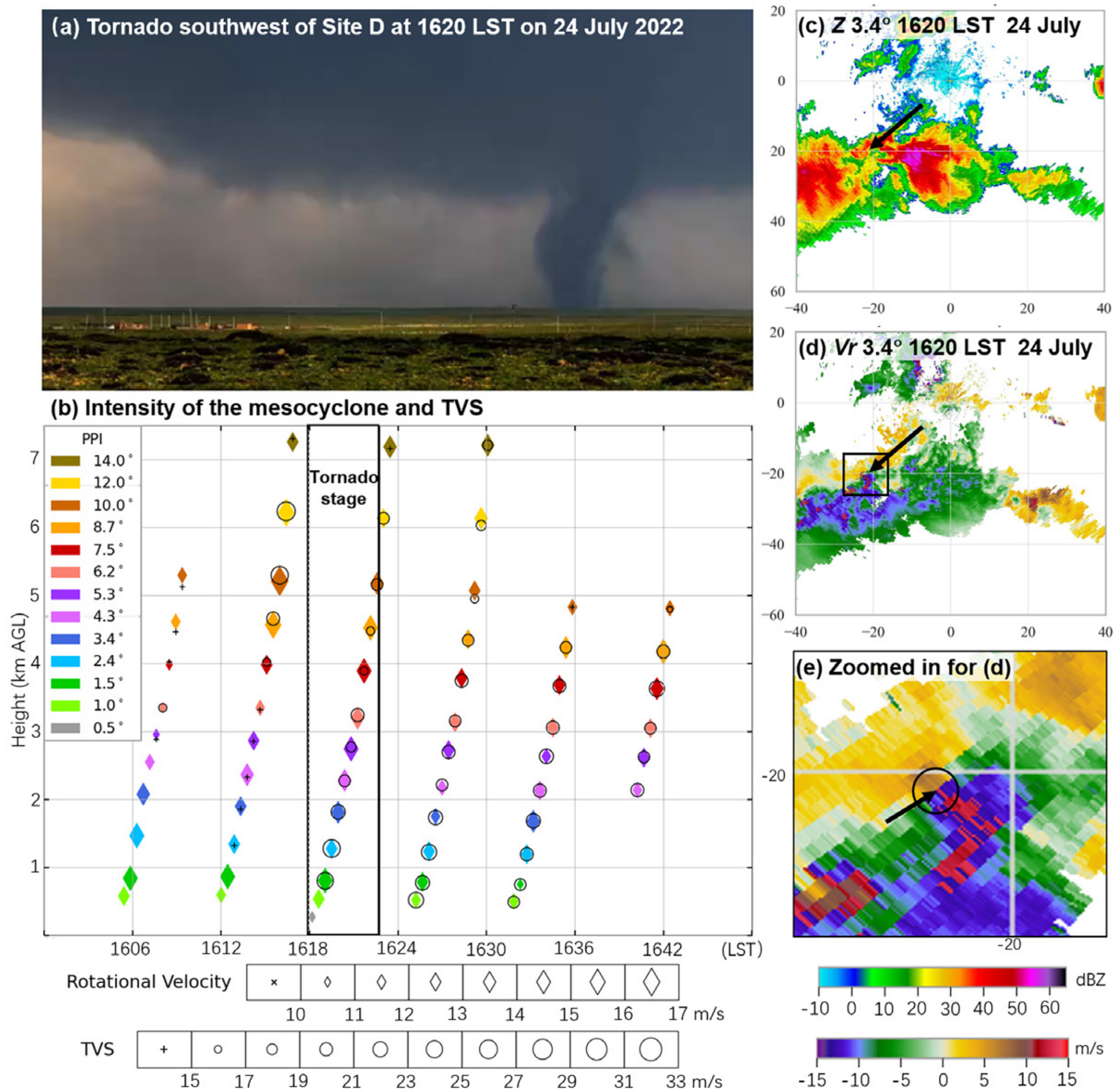

Fig. 19. (a) The tornado that occurred 28 km southwest of site D between 1618 and 1623 LST 24 Jul 2022. (b) The evolution of the rotational velocity (diamond) of the mesocyclone and the maximum gate-to-gate azimuthal radial velocity difference (over an azimuthal distance of one beamwidth) of the tornado vortex signature (TVS) within the mesocyclone, as sampled by the NJU C-POL radar at site D. (c),(d) The reflectivity and radial velocity at the 3.4° elevation, revealing a supercell with a hook echo and a mesocyclone exhibiting a maximum rotational velocity of 16 m s^{-1} and a TVS with a velocity difference of 32 m s^{-1}. (e) Zoomed in on the black box in (d).

moisture and overestimation of sensible heat flux using Noah land surface model similar to Lachenmeier et al. (2024), which resulted in forecast error in capturing BLCL and CI events, suggesting necessity in model refinement, in particular, in land surface model over heterogeneous land cover. Data assimilation and parameter estimation techniques can leverage DECODE observations to enhance model accuracy. Furthermore, the dataset's wealth of radiosonde data enables investigations into BLCL and CI predictability and the impact of targeted observations on forecasting skill.

DECODE observations offer fertile ground for interdisciplinary studies. The presence of extensive wind farms in desert areas near sites B and C may influence BLCL behaviors and their CIs, an aspect that has received limited attentions thus far, although there have been many efforts in examining wake turbulence (e.g., Baidya Roy and Traiteur 2010; Zhou et al. 2012) and parameterization in numerical models (e.g., Fitch et al. 2012; Fitch 2015). Furthermore, observations of blowing dust associated with gust fronts during DECODE offer an opportunity to study convective dust events in desert regions adjacent to oases, where thunderstorms and gust fronts are prevalent. Relative to large-scale dust events, convective dust events are emerging as a hot interdisciplinary topic.

The DECODE campaign demonstrated that effective convection-resolving real-time numerical prediction, coupled with proficient nowcasting support at the operation center and seamless communication, proved crucial for planning aircraft operations and implementing system-following strategies, such as portable radiosondes. The preconfigured WRF Model, with a 1-km resolution, demonstrated reliable prediction of BLCL formation, playing a pivotal role in operational planning. Real-time displays of surface observations and radar data, along with the *FY-4B* GHI satellite image animation, were essential for monitoring BLCL and CI and thus deploying mobile instruments. The use of WeChat facilitated efficient communication among people at the operation center, different sites, and mobile teams. However, a significant coordination challenge arose from the simultaneous deployment of radiosondes beyond site areas. In desert regions, weak or intermittent internet connectivity posed obstacles to instrument redeployment in response to changing weather conditions. It is hoped that technologies like Starlink could be employed in future campaigns, particularly in inhabitant areas.

The execution of the DECODE campaign broadened the scope of local operational forecasting practices. Prior to DECODE, the phenomena of BLCLs and their roles in CI were not fully recognized in local operational forecast services. Following DECODE, local meteorological observatories began incorporating observations of clear-air fine lines to anticipate storm initiation locations, supplementing radar-based nowcasting efforts after storm initiation. The occurrences of BLCLs over the desert, occasionally extending into the oasis, shed light on the climatologically higher frequency of convection in the eastern oasis. This was evidenced by the distribution of lightning frequencies from June to August during the period 2014–23 (Fig. 20a), with BLCL-associated lightning dominating (Fig. 20b vs Fig. 20c). Understanding the characteristics of BLCLs is crucial for contextualizing situations where convection was forecasted across the entire oasis under favorable synoptic-scale conditions, yet only manifested in the eastern oasis. Moreover, the deployment of observational facilities during DECODE provided valuable insights for potentially enhancing the observational network in the Hetao area.

Numerous ongoing works, led by the authors of this paper and other researchers, continue to delve into case studies, composite analyses, model verification and improvement, data assimilation, and predictability. These endeavors, focusing on land–atmosphere interactions, boundary layer processes, and MCS dynamics and microphysics, aim to deepen our understanding of the interaction between land surface characteristics and atmospheric dynamics. Ultimately, these efforts will bolster our capacity to forecast and

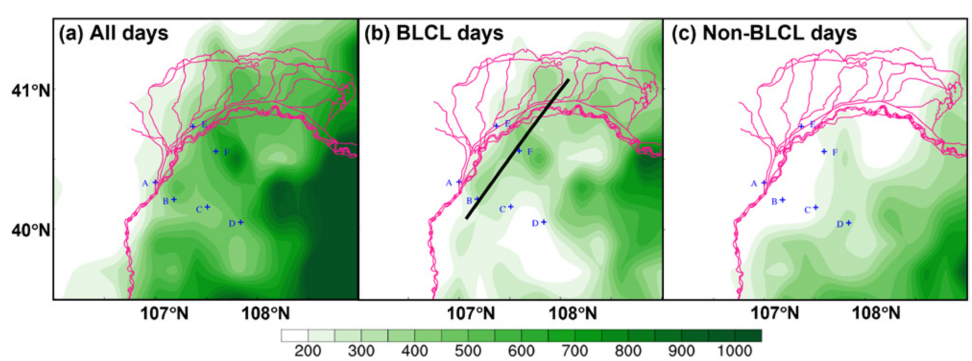

Fig. 20. **Distribution of lightning frequencies from June to August over the period 2014–23, showcasing (a) all days, (b) BLCL days, and (c) non-BLCL days. The black line denotes the typical location of BLCLs. The purple background contours denote the Yellow River and irrigation canals.**

mitigate convective weather hazards in regions characterized by heterogeneous terrain in arid and semi-arid climate regimes.

Acknowledgments. The DECODE campaign would have been impossible without the dedication of ~100 participants. Their collaborative spirit was exemplary, particularly given the harsh desert conditions and the ongoing COVID-19 pandemic. Invaluable assistance and unwavering commitment of numerous individuals and organizations are appreciated. First and foremost, we extend our sincere gratitude to the NSFC42030604 for providing funding crucial to the campaign's execution. We appreciate the insightful suggestions on project design and implementation provided by Jianfang Fei, Hongsheng Zhang, Haishan Chen, Zeyong Hu, Mingxuan Chen, Jie Tang, and Bowen Zhou. We would like to express our special thanks to the Inner Mongolia Meteorological Bureau for their support in various aspects, including site exploration, deployment of forecasters during rainy season, and organizing aircraft reconnaissance missions. We also acknowledge the support of the Bayannur Meteorological Bureau of Inner Mongolia, the Linhe District Meteorological Bureau of Bayannur, the Dengkou County Meteorological Bureau of Bayannur, the Yihewusu National Basic Meteorological Observing Station, the Wuhai Meteorological Bureau of Inner Mongolia, Nanjing University, and the Baotou Meteorological Bureau of Inner Mongolia for their assistance in setting up observation sites, deploying radars, and conducting radiosonde observations. We are grateful to Qingdao Huahang Seaglet Environmental Technology Co., Ltd. and North Sky Dome Information Technology (Xi'an) Co., Ltd. for their support in deploying and training on microwave radiometers and Doppler lidars. Special thanks are also due to the Eighth Branch of Ordos City Highway Toll Collection Service Center for providing observation sites, as well as to GD (Guodian) Power Inner Mongolia New Energy Development Co., Ltd., Bayin Engel, and Chaganbaixing Yurt for their contributions to site setup. Last but not the least, we are deeply grateful for the support and collaboration from the Desert Forestry Experimental Center of the Chinese Academy of Forestry.

Data availability statement. *FY-4B* GHI satellite data, lightning data, surface observations, and Linhe radar data were provided by the National Meteorological Information Center of the China Meteorological Administration (https://data.cma.cn/data/cdcindex/cid/0b9164954813c573.html). The ERA5 data used in this work (Hersbach et al. 2018a,b for data on pressure and single levels) are freely available on the Copernicus Data Store (CDS) at https://cds.climate.copernicus.eu/cdsapp#!/search?type=dataset. The MODIS data (MOD13A3-V006; Didan 2015) were downloaded from NASA's Earth Observing System Data and Information System (EOSDIS; https://search.earthdata.nasa.gov/search). The DECODE observation data are available from the corresponding author upon reasonable request. This dataset will become publicly available for research purpose after checking compliance with the requirement demanded by local regulations. The DECODE 30-min documentary "STORM CHASING 48 DAYS" and its 90-s trailer, some time-lapse videos of boundary layer convergence lines, storms, tornadoes, and gust fronts are publicly available at https://opendata.pku.edu.cn/dataverse/DECODE_VIDEO_CATALOG.

References

André, J.-C., J.-P. Goutorbe, and A. Perrier, 1986: HAPEX—MOBLIHY: A hydrologic atmospheric experiment for the study of water budget and evaporation flux at the climatic scale. *Bull. Amer. Meteor. Soc.*, **67**, 138–144, https://doi.org/10.1175/1520-0477(1986)067<0138:HAHAEF>2.0.CO;2.

Baidya Roy, S., and J. J. Traiteur, 2010: Impacts of wind farms on surface air temperatures. *Proc. Natl. Acad. Sci. USA*, **107**, 17 899–17 904, https://doi.org/10.1073/pnas.1000493107.

Banghoff, J. R., J. D. Sorber, D. J. Stensrud, G. S. Young, and M. R. Kumjian 2020: A 10-year warm-season climatology of horizontal convective rolls and cellular convection in central Oklahoma. *Mon. Wea. Rev.*, **148**, 21–42, https://doi.org/10.1175/MWR-D-19-0136.1.

Barton, E. J., and Coauthors, 2020: A case-study of land–atmosphere coupling during monsoon onset in Northern India. *Quart. J. Roy. Meteor. Soc.*, **146**, 2891–2905, https://doi.org/10.1002/qj.3538.

Boone, A., and Coauthors, 2021: Updates on the international land surface interactions with the atmosphere over the Iberian Semi-Arid Environment (LIAISE) field campaign. 6 pp., https://hal.science/hal-03842003/document.

Brooke, J. K., and Coauthors, 2024: Irrigation contrasts through the morning transition. *Quart. J. Roy. Meteor. Soc.*, **150**, 170–194, https://doi.org/10.1002/qj.4590.

Chug, D., F. Dominguez, C. M. Taylor, C. Klein, and S. W. Nesbitt, 2023: Dry-to-wet soil gradients enhance convection and rainfall over subtropical South America. *J. Hydrometeor.*, **24**, 1563–1581, https://doi.org/10.1175/JHM-D-23-0031.1.

Didan, K., 2015: MOD13A3 MODIS/Terra vegetation Indices Monthly L3 Global 1km SIN Grid V006. NASA EOSDIS Land Processes DAAC, accessed 10 October 2019, https://doi.org/10.5067/MODIS/MOD13A3.006.

Doran, J. C., and Coauthors, 1992: The Boardman regional flux experiment. *Bull. Amer. Meteor. Soc.*, **73**, 1785–1795, https://doi.org/10.1175/1520-0477(1992)073<1785:TBRFE>2.0.CO;2.

Fitch, A. C., 2015: Climate impacts of large-scale wind farms as parameterized in a global climate model. *J. Climate*, **28**, 6160–6180, https://doi.org/10.1175/JCLI-D-14-00245.1.

——, J. B. Olson, J. K. Lundquist, J. Dudhia, A. K. Gupta, J. Michalakes, and I. Barstad, 2012: Local and mesoscale impacts of wind farms as parameterized in a mesoscale NWP model. *Mon. Wea. Rev.*, **140**, 3017–3038, https://doi.org/10.1175/MWR-D-11-00352.1.

Froidevaux, P., L. Schlemmer, J. Schmidli, W. Langhans, and C. Schär, 2014: Influence of the background wind on the local soil moisture–precipitation feedback. *J. Atmos. Sci.*, **71**, 782–799, https://doi.org/10.1175/JAS-D-13-0180.1.

Han, Y., and Coauthors, 2017: Development and application of new boundary layer meteorological sounding system (in Chinese). *Qixiang Keji*, **45**, 804–810.

Hersbach, H., and Coauthors, 2018a: ERA5 hourly data on pressure levels from 1959 to present. Copernicus Climate Change Service (C3S) Climate Data Store (CDS), accessed 10 October 2019, https://cds.climate.copernicus.eu/cdsapp#!/search?type=dataset.

——, and Coauthors, 2018b: ERA5 hourly data on single levels from 1959 to present. Copernicus Climate Change Service (C3S) Climate Data Store (CDS), accessed 10 October 2019, https://cds.climate.copernicus.eu/cdsapp#!/search?type=dataset.

Huang, Y., Z. Meng, W. Li, L. Bai, and X. Meng, 2019: General features of radar-observed boundary layer convergence lines and their associated convection over a sharp vegetation-contrast area. *Geophys. Res. Lett.*, **46**, 2865–2873, https://doi.org/10.1029/2018GL081714.

——, ——, and M. Zhang, 2022: Synoptic impacts on the occurrence of mesoscale boundaries and their associated convection over an area of sharp vegetation contrast. *Geophys. Res. Lett.*, **49**, e2022GL099449, https://doi.org/10.1029/2022GL099449.

Jolliffe, I. T., and D. B. Stephenson, 2003: *Forecast Verification: A Practitioner's Guide in Atmospheric Science.* John Wiley and Sons, 240 pp.

Kang, S.-L., and G. H. Bryan, 2011: A large-eddy simulation study of moist convection initiation over heterogeneous surface fluxes. *Mon. Wea. Rev.*, **139**, 2901–2917, https://doi.org/10.1175/MWR-D-10-05037.1.

——, and J.-H. Ryu, 2016: Response of moist convection to multi-scale surface flux heterogeneity. *Quart. J. Roy. Meteor. Soc.*, **142**, 2180–2193, https://doi.org/10.1002/qj.2811.

Kawase, H., T. Yoshikane, M. Hara, F. Kimura, T. Sato, and S. Ohsawa, 2008: Impact of extensive irrigation on the formation of cumulus clouds. *Geophys. Res. Lett.*, **35**, L01806, https://doi.org/10.1029/2007GL032435.

Klein, C., and C. M. Taylor, 2020: Dry soils can intensify mesoscale convective systems. *Proc. Natl. Acad. Sci. USA*, **117**, 21 132–21 137, https://doi.org/10.1073/pnas.2007998117.

Klemp, J. B., 1987: Dynamics of tornadic thunderstorms. *Annu. Rev. Fluid Mech.*, **19**, 369–402, https://doi.org/10.1146/annurev.fl.19.010187.002101.

Kumjian, M. R., O. P. Prat, K. J. Reimel, M. van Lier-Walqui, and H. C. Morrison, 2022: Dual-polarization radar fingerprints of precipitation physics: A review. *Remote Sens.*, **14**, 3706, https://doi.org/10.3390/rs14153706.

Lachenmeier, E., and Coauthors, 2024: Irrigated agriculture significantly modifies seasonal boundary layer atmosphere and lower-tropospheric convective environment. *J. Appl. Meteor. Climatol.*, **63**, 245–262, https://doi.org/10.1175/JAMC-D-23-0020.1.

Lee, J. M., Y. Zhang, and S. A. Klein, 2019: The effect of land surface heterogeneity and background wind on shallow cumulus clouds and the transition to deeper convection. *J. Atmos. Sci.*, **76**, 401–419, https://doi.org/10.1175/JAS-D-18-0196.1.

Liu, H., Z. Meng, Y. Zhu, and Y. Huang, 2023: Convection initiation associated with a boundary layer convergence line over a real-world sharp vegetation-contrast area. *Mon. Wea. Rev.*, **151**, 1189–1212, https://doi.org/10.1175/MWR-D-22-0083.1.

Lunel, T., A. A. Boone, and P. Le Moigne, 2024: Irrigation strongly influences near-surface conditions and induces breeze circulation: Observational and model-based evidence. *Quart. J. Roy. Meteor. Soc.*, **150**, 2798–2819, https://doi.org/10.1002/qj.4736.

Mahmood, R., K. G. Hubbard, and C. Carlson, 2004: Modification of growing-season surface temperature records in the Northern Great Plains due to land-use transformation: Verification of modelling results and implication for global climate change. *Int. J. Climatol.*, **24**, 311–327, https://doi.org/10.1002/joc.992.

——, S. A. Foster, T. Keeling, K. G. Hubbard, C. Carlson, and R. Leeper, 2006: Impacts of irrigation on 20th century temperature in the northern Great Plains. *Global Planet. Change*, **54** (1–2), 1–18, https://doi.org/10.1016/j.gloplacha.2005.10.004.

——, T. Keeling, S. A. Foster, and K. G. Hubbard, 2013: Did irrigation impact 20th century air temperature in the High Plains aquifer region? *Appl. Geogr.*, **38**, 11–21, https://doi.org/10.1016/j.apgeog.2012.11.002.

Mahrt, L., J. Sun, J. I. Dean Vickers, J. R. Pederson, and R. L. Desjardins, 1994: Observations of fluxes and inland breezes over a heterogeneous surface. *J. Atmos. Sci.*, **51**, 2484–2499, https://doi.org/10.1175/1520-0469(1994)051<2484:OOFAIB>2.0.CO;2.

Parker, M. D., and R. H. Johnson, 2000: Organizational modes of midlatitude mesoscale convective systems. *Mon. Wea. Rev.*, **128**, 3413–3436, https://doi.org/10.1175/1520-0493(2001)129<3413:OMOMMC>2.0.CO;2.

Phillips, C. E., U. S. Nair, R. Mahmood, E. Rappin, and R. A. Pielke Sr., 2022: Influence of irrigation on diurnal mesoscale circulations: Results from GRAINEX. *Geophys. Res. Lett.*, **49**, e2021GL096822, https://doi.org/10.1029/2021GL096822.

Purdom, J. F. W., 1976: Some uses of high-resolution GOES imagery in the mesoscale forecasting of convection and its behavior. *Mon. Wea. Rev.*, **104**, 1474–1483, https://doi.org/10.1175/1520-0493(1976)104<1474:SUOHRG>2.0.CO;2.

Rappin, E., and Coauthors, 2021: The Great Plains Irrigation Experiment (GRAINEX). *Bull. Amer. Meteor. Soc.*, **102**, E1756–E1785, https://doi.org/10.1175/BAMS-D-20-0041.1.

Rappin, E. D., R. Mahmood, U. S. Nair, and R. A. Pielke Sr., 2022: Land–atmosphere interactions during GRAINEX: Planetary boundary layer evolution in the presence of irrigation. *J. Hydrometeor.*, **23**, 1401–1417, https://doi.org/10.1175/JHM-D-21-0160.1.

Redelsperger, J.-L., C. D. Thorncroft, A. Diedhiou, T. Lebel, D. J. Parker, and J. Polcher, 2006: African monsoon multidisciplinary analysis: An international research project and field campaign. *Bull. Amer. Meteor. Soc.*, **87**, 1739–1746, https://doi.org/10.1175/BAMS-87-12-1739.

Rochetin, N., F. Couvreux, and F. Guichard, 2017: Morphology of breeze circulations induced by surface flux heterogeneities and their impact on convection initiation. *Quart. J. Roy. Meteor. Soc.*, **143**, 463–478, https://doi.org/10.1002/qj.2935.

Rosenfeld, D., and R. Nirel, 1996: Seeding effectiveness—The interaction of desert dust and the southern margins of rain cloud systems in Israel. *J. Appl. Meteor.*, **35**, 1502–1510, https://doi.org/10.1175/1520-0450(1996)035<1502:SEIODD>2.0.CO;2.

Sato, T., F. Kimura, and A. S. Hasegawa, 2007: Vegetation and topographic control of cloud activity over arid/semiarid Asia. *J. Geophys. Res.*, **112**, D24109, https://doi.org/10.1029/2006JD008129.

Schaefer, V. J., 1949: The formation of ice crystals in the laboratory and the atmosphere. *Chem. Rev.*, **44**, 291–320, https://doi.org/10.1021/cr60138a004.

——, 1954: The concentration of ice nuclei in air passing the summit of Mt. Washington. *Bull. Amer. Meteor. Soc.*, **35**, 310–314, https://doi.org/10.1175/1520-0477-35.7.310.

Segal, M., and R. W. Arritt, 1992: Nonclassical mesoscale circulations caused by surface sensible heat-flux gradients. *Bull. Amer. Meteor. Soc.*, **73**, 1593–1604, https://doi.org/10.1175/1520-0477(1992)073<1593:NMCCBS>2.0.CO;2.

Sellers, P. J., F. G. Hall, G. Asrar, D. E. Strebel, and R. E. Murphy, 1988: The First ISLSCP Field Experiment (FIFE). *Bull. Amer. Meteor. Soc.*, **69**, 22–27, https://doi.org/10.1175/1520-0477(1988)069<0022:TFIFE>2.0.CO;2.

Stensrud, D. J., G. S. Young, and M. R. Kumjian, 2022: Wide horizontal convective rolls over land. *Mon. Wea. Rev.*, **150**, 2999–3010, https://doi.org/10.1175/MWR-D-22-0014.1.

Taylor, C. M., 2015: Detecting soil moisture impacts on convective initiation in Europe. *Geophys. Res. Lett.*, **42**, 4631–4638, https://doi.org/10.1002/2015GL064030.

——, D. J. Parker, and P. P. Harris, 2007: An observational case study of mesoscale atmospheric circulations induced by soil moisture. *Geophys. Res. Lett.*, **34**, L15801, https://doi.org/10.1029/2007GL030572.

——, R. A. M. de Jeu, F. Guichard, P. P. Harris, and W. A. Dorigo, 2012: Afternoon rain more likely over drier soils. *Nature*, **489**, 423–426, https://doi.org/10.1038/nature11377.

Taylor, N. M., and Coauthors, 2011: The understanding severe thunderstorms and Alberta boundary layers experiment (UNSTABLE) 2008. *Bull. Amer. Meteor. Soc.*, **92**, 739–763, https://doi.org/10.1175/2011BAMS2994.1.

Turner, A. G., and Coauthors, 2020: Interaction of convective organization with monsoon precipitation, atmosphere, surface and sea: The 2016 INCOMPASS field campaign in India. *Quart. J. Roy. Meteor. Soc.*, **146**, 2828–2852, https://doi.org/10.1002/qj.3633.

Udina, M., E. Peinó, F. Polls, J. Mercader, I. Guerrero, A. Valmassoi, A. Paci, and J. Bech, 2024: Irrigation impact on boundary layer and precipitation characteristics in Weather Research and Forecasting model simulations during LIAISE-2021. *Quart. J. Roy. Meteor. Soc.*, **150**, 3251–3273, https://doi.org/10.1002/qj.4756.

Wang, J. M., 1999: Land surface process experiments and interaction study in China: From HEIFE to IMGRASS and GAME-Tibet/Tipex (in Chinese, with English abstract). *Plateau Meteor.*, **18**, 280–294.

Weckwerth, T. M., and Coauthors, 2004: An overview of the International H_2O Project (IHOP_2002) and some preliminary highlights. *Bull. Amer. Meteor. Soc.*, **85**, 253–278, https://doi.org/10.1175/BAMS-85-2-253.

Whitesel, D., R. Mahmood, P. Flanagan, E. Rappin, U. Nair, R. A. Pielke Sr., and M. Hayes, 2024: Impacts of irrigation on a precipitation event during GRAINEX in the High Plains Aquifer region. *Agric. For. Meteor.*, **345**, 109854, https://doi.org/10.1016/j.agrformet.2023.109854.

Wilks, D. S., 1995: *Statistical Methods in the Atmospheric Sciences: An Introduction.* Academic Press, 467 pp.

Wilson, J. W., and W. E. Schreiber, 1986: Initiation of convective storms at radar-observed boundary-layer convergence lines. *Mon. Wea. Rev.*, **114**, 2516–2536, https://doi.org/10.1175/1520-0493(1986)114<2516:IOCSAR>2.0.CO;2.

Yuan, S., Y. Wang, S. M. Quiring, T. W. Ford, and A. L. Houston, 2020: A sensitivity study on the response of convection initiation to in situ soil moisture in the central United States. *Climate Dyn.*, **54**, 2013–2028, https://doi.org/10.1007/s00382-019-05098-0.

Zhang, M., and Z. Meng, 2019: Warm-sector heavy rainfall in southern China and its WRF simulation evaluation: A low-level-jet perspective. *Mon. Wea. Rev.*, **147**, 4461–4480, https://doi.org/10.1175/MWR-D-19-0110.1.

Zhou, L., Y. Tian, S. Baidya Roy, C. Thorncroft, L. F. Bosart, and Y. Hu, 2012: Impacts of wind farms on land surface temperature. *Nat. Climate Change*, **2**, 539–543, https://doi.org/10.1038/nclimate1505.

Zhu, P., and Coauthors, 2018: Comparison of three kinds of wind data in boundary layers under complex surface conditions in Beijing (in Chinese). *J. Arid Meteor.*, **36**, 794–801.